



Insights into the formation of Shihuiyao Ta-Nb deposit in southern Great Xing'an Range, NE China: Evidence from chronology and fluid inclusion

Xinkai Chen^a, Zhenhua Zhou^{a,b,*}, Xu Gao^{a,c}, Jiaqi Zhao^a

^a MNR Key Laboratory of Metallogeny and Mineral Assessment, Institute of Mineral Resources, CAGS, Beijing 100037, China

^b Research School of Earth Sciences, Australian National University, Canberra, ACT 2601, Australia

^c Institut für Mineralogie, Leibniz Universität Hannover, Callinstr. 3, 30167 Hannover, Germany



ARTICLE INFO

Keywords:

Hydrothermal process
Fluid inclusions
Water-rock interaction
Fluid boiling and mixing
Tin mineralization

ABSTRACT

Shihuiyao is a typical granite-type Ta-Nb deposit in the southern Great Xing'an Range (SGXR), Northeast China. The ore field is comprised of several granitic intrusions that were emplaced into the Early Permian Linxi Formation during the Late Jurassic (ca. 145 ~ 150 Ma). The main Ta-Nb mineralization (stage 1–2) is found within the leucogranite, with minor identified in the porphyritic granite in the deposit. Four distinct stages in the metallogenetic process can be identified: weakly mineralized magmatic stage (stage 1), strongly mineralized magmatic stage (stage 2), post-magmatic hydrothermal stage (stage 3) and low-temperature hydrothermal stage (stage 4). Cassiterite samples collected from stage 2 were dated to be 147 ± 3.5 Ma and 147.7 ± 1.9 Ma, providing evidence for the latest Jurassic Ta-Nb metallogenetic event at Shihuiyao. To acquire a more profound comprehension of the properties and behaviors of the fluids, fluid inclusions within quartz, albite, amazonite and fluorite were analyzed among all stages. The results showed that the Shihuiyao fluid inclusions were relatively homogeneous and predominantly comprised liquid-rich inclusions, with occasional occurrences of CO₂-type, vapor-rich type, and solid-type inclusions. From stage 1 to stage 4, the temperature of the ore-forming fluids decreased gradually, while the salinity showed increasing during stage 4, which indicates a possible contribution from surrounding strata sourced fluids. Raman analysis of the inclusions at each stage revealed that the vapor components were primarily H₂O, CO₂, and CH₄, with additional N₂ and CH₄ appearing in the late stage, pointing to mixing between the metallogenetic fluids and the surrounding strata source materials. Notably, the simultaneous occurrence of liquid-rich and solid-type inclusions under low pressure conditions (0.6 ~ 1.5 km) in the early ore-forming stage (stages 1–2) suggests a fluid boiling process. We argue that the fluid boiling and rapid chemical quenching of the granitic melt play a crucial role in changing the physicochemical conditions of the ore-forming fluids, ultimately resulting in the enrichment and precipitation of niobium and tantalum. The fluid mixing and intense water–rock interaction in the late stages (stages 3–4) may have also contributed to the minor mineralization.

Drawing upon our investigations utilizing petrographic features and composition analysis of individual fluid inclusions, we have prognosticated on the Sn mineralization potential within the Shihuiyao deposit. Our results indicate the Shihuiyao granites are comparable to the tin granites worldwide. Genesis of cassiterites is linked to both magmatic and hydrothermal processes, exsolution from tin-rich fluids (up to 233 ppm) and interaction with country rocks attribute to the probable economic tin mineralization. Consequently, the Shihuiyao deposit has been noteworthy prospectively for further tin mineralization.

1. Introduction

Niobium and tantalum play an essential role in clean energy, photovoltaic cells, aerospace and other fields, which serve as important raw materials for fabricating high-tech equipment (Jiang et al., 2019;

Zhai et al., 2019a; Zhai et al., 2019b). Although there has been some advancement in the classification of Nb-Ta deposits and their tectonic settings in recent years (Cerný et al., 1992; Linnen et al., 2014), there is still a major controversy on the genesis of these deposits. such as the main mechanism for mineral precipitation. Conventionally, Nb-Ta

* Corresponding author at: 142 Mills Rd, Research School of Earth Sciences, Australian National University, Canberra, ACT 2601, Australia.

E-mail address: zhzhoucags@sina.com (Z. Zhou).

deposits are considered of magmatic origin, pivotal factor responsible for their mineralization is the preferential accumulation and subsequent crystallization of ore-forming elements (Nb, Ta) during the final stages of magmatic fractionation (Pichavant et al., 1988; Yin et al., 1995; Chevychelov et al., 2005). However, a series of studies recently have indicated that Nb-Ta deposits may also have a hydrothermal origin, hydrothermal alteration or fluid metasomatism was essential for the formation of Nb-Ta deposits (Wu et al., 2018; Zhou et al., 2022). Besides, Pollard's recent proposal of alternative evolutionary mechanisms highlights the critical role of volatiles in niobium and tantalum deposits (Pollard, 2021). In addition, the current understanding and research on the enrichment mechanism of associated metallogenic elements (e.g., Li, Sn, W, etc.) in Nb-Ta deposits, as well as the scale of mineralization, remain insufficient. This limitation significantly impedes the economic value of deposit exploration and development.

Fluid inclusions (FIs) in ore-bearing rocks could provide evidence for the genesis of granites and ores, which is the direct embodiment of paleo-fluid composition (Fan et al., 2003; Audéat, 2019). Using fluid inclusions to invert ore-forming temperature, pressure, and other factors is of critical in determining the source and evolution of mineralized fluids. This approach offers a unique perspective on the precipitation mechanisms of ore minerals and provides valuable insights into their formation processes (Audéat et al., 1998; Pan et al., 2019; Shu et al., 2021). Since the turn of the 21st century, there has been a rapid

advancement in individual fluid inclusion analysis, which has enabled researchers to discern mineralization events and even evaluate mineralization potential with greater precision (Audéat et al., 2000; Heinrich et al., 2003; Han et al., 2023). Moreover, innovation in analytical chemistry makes it widespread-used for U-Pb dating in some accessory minerals (e.g., cassiterite, columbite) (Yuan et al., 2011; Che et al., 2015). Regarding cassiterite, its U-Pb isotope system is capable of maintaining closure even during the late hydrothermal stage, owing to its high closure temperature which exceeds the mineralized temperature (Zhang et al., 2011; Neymark et al., 2018). Cassiterite also tends to possess higher U and lower common Pb contents, and effectively preserves U and radiogenic Pb within the crystal lattice, is consequently extensively employed for dating rare metal deposits (Lehmann et al., 2020).

Shihuiyao Ta-Nb deposit is situated in the southern Great Xing'an Range (SGXR) (Fig. 1), with estimated resources of 16.21 Mt. Nb₂O₅ and Ta₂O₅, and average ore grades of 0.02% Nb₂O₅ and 0.015% Ta₂O₅ (Zhou et al., 2022). Antecedent researches on the deposit have concentrated on the genesis of ore-forming rocks and ore minerals, geochronology, and the establishment of metallogenic model (Sun et al., 2015; Duan et al., 2021, 2022; Zhou et al., 2022). However, evolution of the ore-forming fluids and precipitation mechanism of ore minerals in the metallogenic process are still obscure. Furthermore, while past research has commonly estimated the mineralization age based on the age of

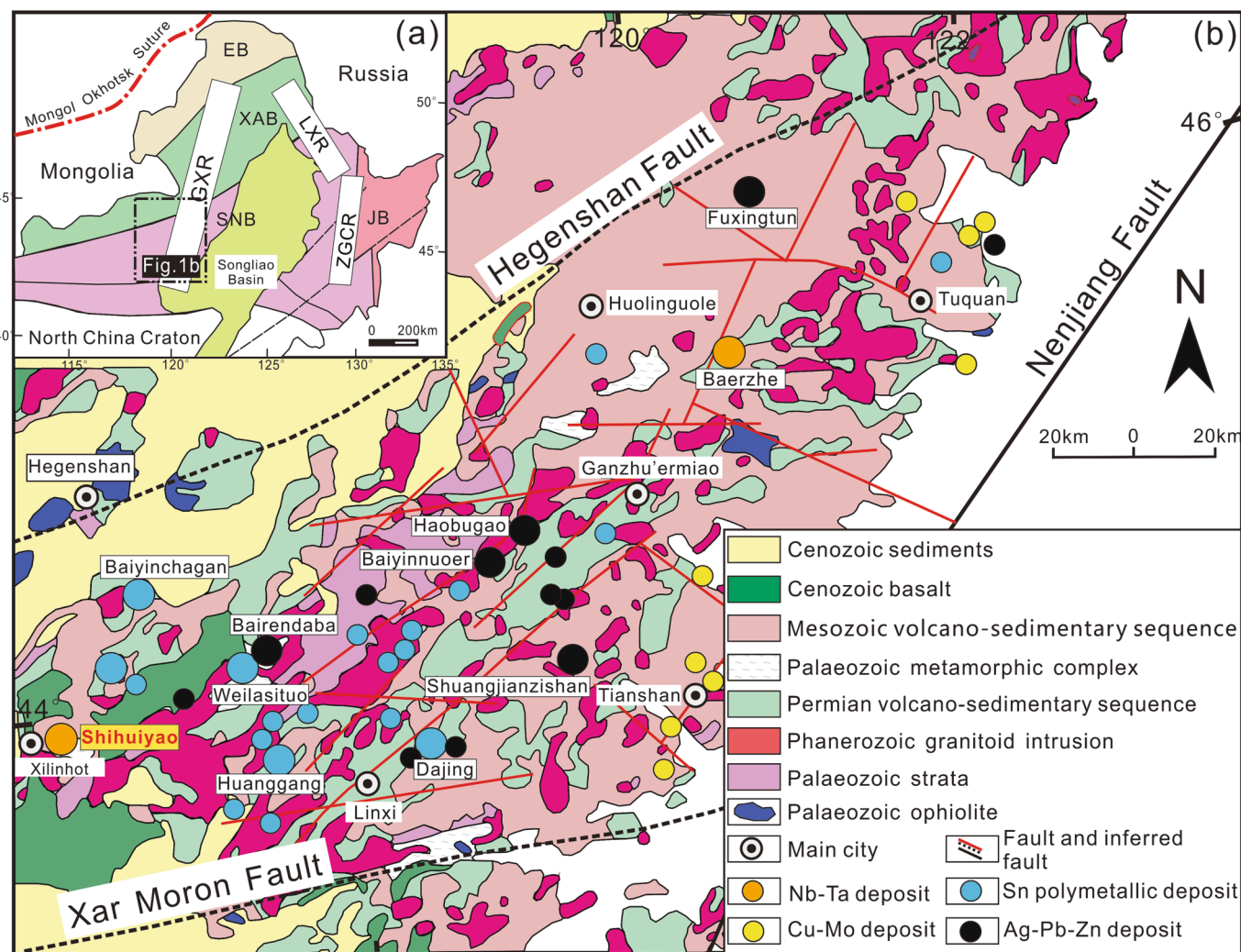


Fig. 1. (a) Simplified geotectonic division of the northeastern China; (b) Geological and ore deposit distribution map of southern Great Xing'an Range (modified after Ouyang et al., 2015). Abbreviations: GXR- Great Xing'an Range; LXR- Lesser Xing'an Range; ZGCR- Zhangguangcai Range; EB-Erguna Block; XAB-Xing'an Block; SNB-Songnen Block; JB-Jiamusi Block.

hydrothermally altered minerals (such as muscovite) that are associated with the ore minerals (Sun et al., 2015; Zhou et al., 2022), the metallogenic age determined from the ore minerals has been reported only by Zhou et al. (2022). Additional research and verification are required to accurately determinate the metallogenic age of this deposit.

Here, we offer petrographic observations, fluid inclusion and cassiterite in situ U-Pb dating data, to (1) elucidate the ore-forming processes of hydrothermal fluids and the precipitation mechanism of the ore minerals, (2) further decipher the metallogenic age of the deposit, in order to enrich our understanding of the deposit, and (3) discuss the prospect of tin mineralization in the Shihuiyao mining area.

2. Regional geology

The Central Asian Orogenic Belt (CAOB) is the largest accretionary orogenic belt on the Earth since Phanerozoic, distinguished by prominent growth of juvenile crust and significant regional mineralization (Sengör et al., 1993; Jahn et al., 2000; Xiao et al., 2009). NE China is in the eastern segment of the CAOB, mainly consisting of several micro-continent massifs and Phanerozoic orogenic belts (Xu et al., 2019). The SGXR is positioned in the southwestern region of NE China, with its primary body situated in the Songnen block (Fig. 1b). The SGXR is viewed as the point of intersection of a complicated amalgamation of island arcs, microcontinental blocks, and ancient oceanic crust (Li et al., 2018; Wilde, 2015). Affected by the subduction of the Paleo-Asian Ocean during the Paleozoic, numerous near-E-W trending structural folds were formed in the area, while lots of NEE-NNE trending faults were emerged during the Mesozoic due to the dual tectonic event of subduction of the Mongolia-Okhotsk Ocean and the Paleo-Pacific Ocean (Xu et al., 2013). These Mesozoic faults are superimposed on Paleozoic faults, forming a unique triangular tectonic framework in the SGXR.

The SGXR is covered by extensive Paleozoic and Mesozoic volcanic rocks and corresponding volcanic-sedimentary sequences. The Early Paleozoic Xilingol complex is the most ancient strata, consisting of middle to high-grade metamorphic biotite gneisses with plagioclase amphibolite lenses (Shi et al., 2003; Li et al., 2017a; Li et al., 2017b; Li et al., 2017c). Ordovician-Silurian, Devonian and Carboniferous clastic metamorphic sedimentary units, carbonate rocks and volcanic rocks are developed partially in the study area. Permian volcanic-sedimentary formation includes Dashizhai Formation, Zhesi Formation and Linxi Formation, and the lithology of these strata mainly includes carbonate rocks, sandstones, metasandstones, and intermediate-felsic to intermediate-basic volcanic rocks, which are served as direct contact wall rocks of multiple metal deposits (Zhou and Mao, 2022). And Mesozoic volcanic-sedimentary sequence constitutes the main cover in the SGXR. From bottom to top, it can be divided into Jurassic Hongqi Formation, Wanbao Formation, Xinmin Formation, Manketoubo Formation, Manitu Formation, Cretaceous Baiyingaolao Formation and Meiletu Formation, which consist of volcanic rocks (mainly basalt, trachyandesite, trachyte and rhyolite) and sedimentary rocks (mainly sandstone and siltstone) (Zhang et al., 2010). The Cenozoic strata include Quaternary floating sands, mainly distributed in sedimentary basins and depression basins.

Since the Phanerozoic, the SGXR has exhibited strong magmatism, which can be divided into three stages: Carboniferous-Permian, Triassic, and Late Jurassic-Early Cretaceous (Wu et al., 2011; Ouyang et al., 2015). The Carboniferous-Permian rocks are predominantly found on the west slope of the SGXR, including diorites, tonalites and granodiorites, whose compositions range from tholeiitic calc-alkaline to high-K calc-alkaline, and are thought to have a strong association with the closure of the Paleo-Asian Ocean (Wilde, 2015; Li et al., 2017a; Li et al., 2017b; Li et al., 2017c, 2018). Felsic intrusive rocks, such as two-mica granites, biotite granodiorites, granodiorite porphyries, etc., are the dominant Triassic magmatic rocks among the central-southern region of the SGXR (Ge et al., 2005; Liu et al., 2007; Wu et al., 2011). And Late Jurassic to Early Cretaceous witnessed extensive magmatic activity,

which consisted of the dominant formation of magmatic rocks in the SGXR region. Specifically, volcanic rock assemblages are mainly intermediate-acid and pyroclastic, and the intrusive rock assemblages are mainly granites, granite porphyries, granodiorites, etc. The peak diagenetic age in this stage was about 140 ~ 130 Ma, which was possibly associated with paleo-Pacific plate subduction (Zhou and Mao, 2022). Geochemistry studies show the granitoids in this stage are in intense connection with mantle-derived or juvenile crust materials, which are closely linked to the metal mineralization (Sn-Ag-Pb-Zn, Ta-Nb) in the SGXR (Shao et al., 2010; Zhou et al., 2012).

3. Geology of the Shihuiyao Ta-Nb deposit

The Shihuiyao deposit is located in the western slope of the SGXR, host strata are predominantly Late Permian Linxi Formation and Quaternary gravel (Fig. 2a). Lithology of Linxi Formation mainly contains calcareous slates, *meta*-siltstones and sandstones, which are black in color and lath-shaped, with quartz-vein and pegmatite veins interspersed. Note that the Linxi Formation is also the main wall rock in the Shihuiyao deposit, in accordance with the majority of the rare metal deposits in the SGXR (Zhou and Mao, 2022). The structural framework mainly contains three large-scale NNE-striking and one small-scale NW-striking faults (Fig. 2a), showing the intense tectonic activity of the ore field. The mineral control structures are mainly three NNE-oriented parallel fracture zones (0.5 ~ 9.7 m in length, 30 ~ 220 m in width), consisting of fractured and low-grade metamorphic rocks, with the intrusive magma and mineralized vein bodies predominantly arranged along these faults (Duan et al., 2016; Zhou et al., 2022).

The prevalent type of igneous rocks that can be observed in the Shihuiyao area are quartz monzonite, quartz diorite, porphyritic granite and leucogranite, and abundant NE-trending felsic dikes. Seven Ta-Nb-hosted plutons are delineated, named #I to #VII, and the leucogranites (including altered and greisenized leucogranite) host the major economic mineralization (Zhou et al., 2022). These mineralized granites are located < 300 m below the present surface, intruded into the Permian Linxi Formation with laminated or thick-slabbed shape. In the depth developed two kinds of orebody, one reached industrial mining standard and the other is a submarginal (Fig. 2b). Specifically, a total of seven industrial ore bodies have been traced, which vary in size. The largest, namely V-1, is dominated by Ta-Nb mineralization, with average $\text{Nb}_2\text{O}_5 + \text{Ta}_2\text{O}_5$ grades of 0.015%~0.093% (Duan et al., 2016), which is 1140 m in length and 4 ~ 249 m in depth. The columbite-group minerals (CGMs), with minor cassiterites and REE-bearing minerals, mainly occurs as stockworks and disseminations in leucogranites and their altered counterparts (Fig. 3). The spreading orientation and the occurrence of the ore body is strictly controlled by the leucogranites, and is generally gently-dipping (6 ~ 40°).

Hydrothermal alteration is widespread across the Shihuiyao ore field, with the highest degree of alteration concentrated in/around the mineralized granites. Albitization during the early stages of mineralization is closely associated with the formation of albite metasomatism in K-feldspar (Fig. 3a, c), and massive occurrences of hydrothermal minerals (such as muscovite, quartz) (Fig. 3c-d). On the scale of hand specimens, pneumatohydrothermal minerals, like fluorite and topaz, can be identified, showing the high temperature gas-hydrothermal alteration of greisenization, tourmalization, topazization and amazonization. And as the depth increases, the alteration gradually weakens, suggesting the low grade of ore bodies in the deep. The final stage of alteration involves low-temperature argillic alteration and pyritization, which is characterized by the presence of illite-calcite assemblages, as well as the occurrence of sulfides (such as pyrite, limonite, sphalerite, molybdenite, etc.) that have superimposed upon all preceding alteration types. This phenomenon is primarily concentrated along the fractures.

Through meticulous field work, and combined with indoor rock ore appraisal, we have categorized the deposit into four main mineralization stages. Stage 1 represents early weak magmatic mineralization, with

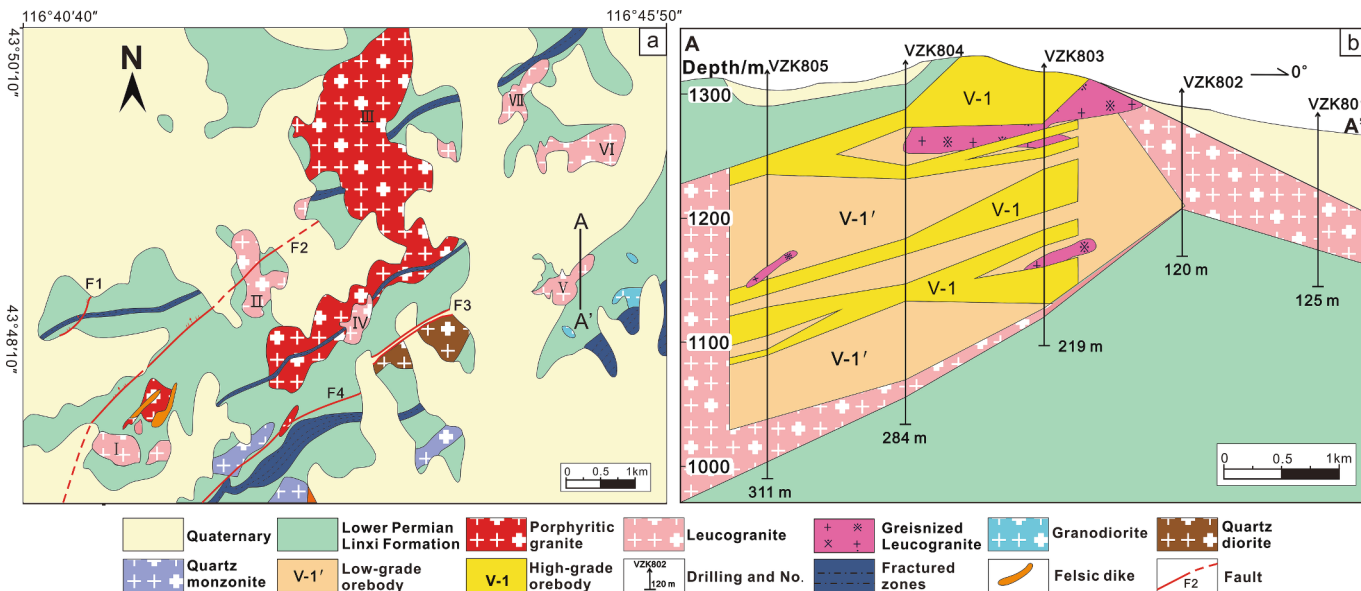


Fig. 2. (a) Geological map of the Shihuiyao Ta-Nb orefield; (b) ore section map of A-A' prospecting line of the Shihuiyao deposit (both modified after Zhou et al., 2022).

minor disseminated Ta-Nb minerals in the porphyritic granites. The main ore-forming stage, *Stage 2*, is marked by robust magmatic mineralization in leucogranites and their altered counterparts, with widespread Ta-Nb mineralization, including pegmatite-type mineralization, the primary ore mineral assemblages are comprised of columbite-group minerals, cassiterite, zinnwaldite and siderophyllite (Fig. 3a-g). *Stage 3* is the post-magmatic hydrothermal stage, which encompasses the sequence of hydrothermal processes at elevated temperatures, characterized by significant thermal alteration and erosion, with the greisenization being the most conspicuous, and the majority of sulfides developed. And during *Stage 4*, the late hydrothermal stage, significant presence of sericite, chlorite, and other medium-to-low temperature alteration minerals could be observed, with minor occurrences of pyrite, limonite, chalcopyrite, monazite, xenotime, and other metal sulfides and/or REE minerals (Fig. 3h-i) (Duan et al., 2020; Zhou et al., 2022).

4. Samples and analytical methods

4.1. LA-ICP-MS cassiterite U-Pb dating

Cassiterites for U-Pb dating were selected from sample XS-2-6 and SHY21-05, whose lithologies were both pegmatites. Cassiterite analyses were conducted on an Analytikjena M90 quadrupole ICPMS with a 193 nm NWR193 Ar-F excimer laser at Yanduzhongshi Geological Analysis Laboratories Ltd. The Pb/U ratios were corrected for downhole fractionation, instrument drift, and mass bias using the primary standard cassiterite Cligga Head and secondary standard cassiterite Emmaville (Prichard, 2013; Tapster and Bright, 2020). Trace element contents were collected using SRM610 as the external standard and ^{118}Sn as the internal standard element. Each analysis on the cassiterite included a 20 s blank gas measurement, followed by 40 s of analysis time with the laser switched on. The isotopes measured included ^{202}Hg , ^{204}Pb , ^{206}Pb , ^{207}Pb , ^{208}Pb , ^{232}Th , and ^{238}U , with each element measured every 0.18 s. The data reduction method used was based on Meffre et al. (2008). And modification to correct for the small amount of common Pb that presented in the primary standard was originated from the ^{207}Pb correction of Chew et al. (2011).

4.2. Microthermometry

Thirty-two double polished sections (~ 200 to $300 \mu\text{m}$ in thickness)

were prepared from 17 samples: (1) five and six quartz phenocryst samples from the mineralization stage 1 and stage 2 respectively; (2) two quartz phenocryst and one fluorite sample from the stage 3; and (3) one fluorite and two quartz samples from the stage 4. Microthermometric measurements of fluid inclusions were conducted using a LINKAM MDSG600 heating-freezing stage attached to a ZEISS microscope at IMR-CAGS. The stage was calibrated using synthetic fluid inclusion standards, ranging from -196 to $+600^\circ\text{C}$. Measurements were taken with a precision of $\pm 0.1^\circ\text{C}$ for ice melting temperature, $\pm 0.5^\circ\text{C}$ for clathrate melting temperature, and $\pm 1^\circ\text{C}$ for homogenization temperature (T_h). To measure the temperature of FIs, freezing/heating rates were kept between 0.2 and $5^\circ\text{C}/\text{min}$, and were lowered to $0.1 \sim 0.5^\circ\text{C}/\text{min}$ when nearing a phase transition. Detailed procedures for fluid inclusion measurements could be found in Shepherd et al. (1985). The apparent salinities for H_2O inclusions are reported as weight percent NaCl equivalent (wt.% NaCl equiv.), and were calculated based on the final ice melting temperature (Bodnar, 1993; Hall et al., 1988). For daughter crystal-bearing H_2O inclusions, salinities were calculated as wt.% NaCl equiv. using final melting temperatures of hydrohalite (Potter et al., 1977). As for salinities for CO_2 -bearing inclusions, were calculated using the melting temperature of CO_2 clathrate and the equations of Bozzo et al. (1973). And bulk densities (g/cm^3) were calculated using Flincor software, based on the microthermometric data of NaCl- H_2O inclusions from Brown and Lamb (1989).

4.3. Laser Raman spectroscopy

Laser Raman spectroscopy was conducted on nearly 20 fluid inclusions at the Beijing Institute of Nuclear Geological Research by LABHR-VIS Lab RAM HR800 microprobe. A yag crystal frequency solid laser with a 532 nm wavelength and 50 MW power was used as the light source. The laboratory conditions were maintained at 25°C and 50% humidity. The scanning wavelength range was 100 to 4200 cm^{-1} .

4.4. Fluid inclusion LA-ICP-MS analysis

LA-ICP-MS was used to analyze individual fluid inclusions within the quartz crystals for their major and trace element compositions. The measurements were carried out at the State Key Laboratory of Mineral Deposit Geochemistry, Institute of Geochemistry, CAS. The resin mold-optimized standard ablation cell facilitates efficient aerosol removal

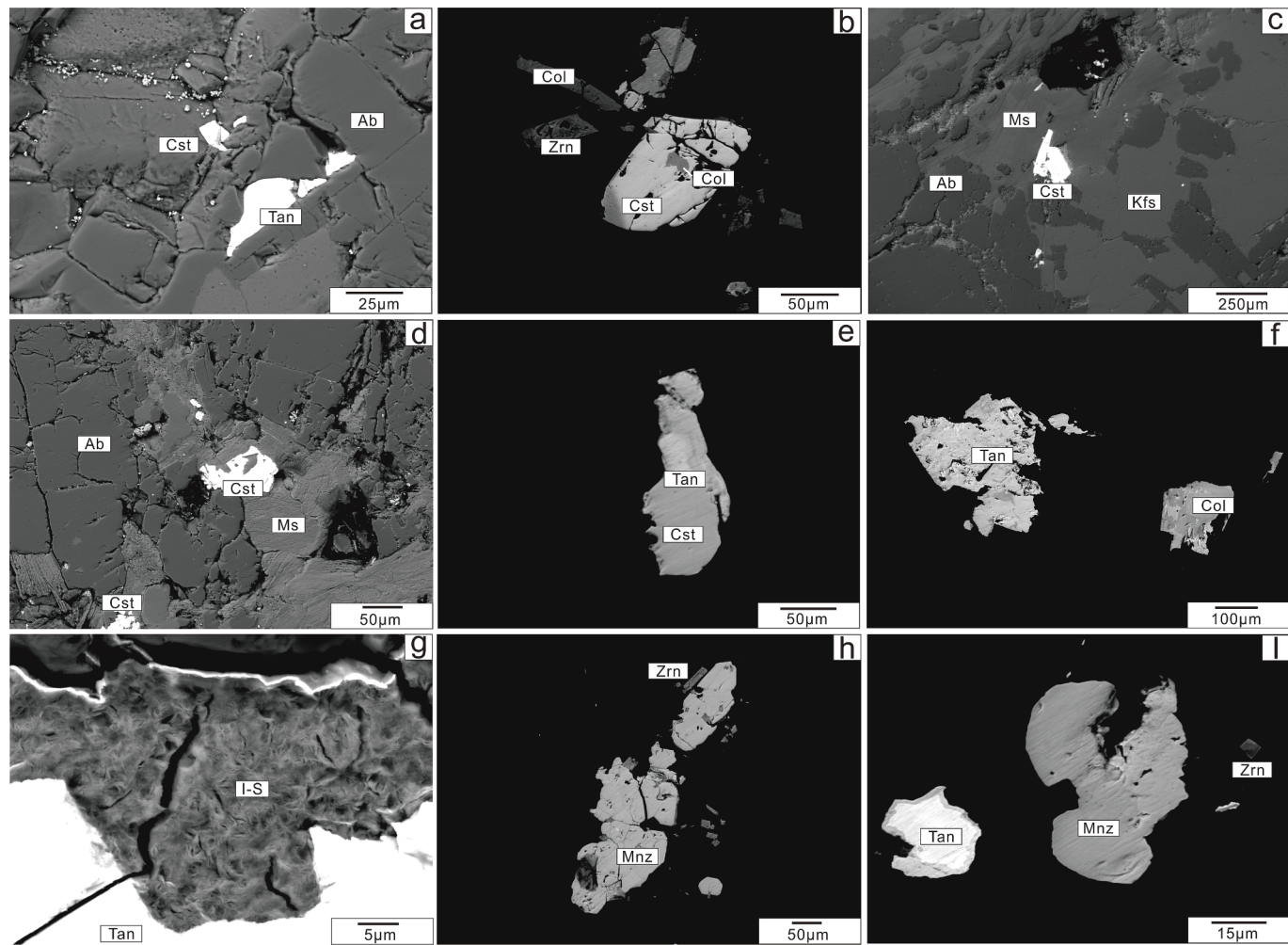


Fig. 3. BSE images in the leucogranites and their altered counterparts. (a-e) show the intimate intergrowth between cassiterite and CGMs or show the subhedral cassiterites enclose the CGMs, the morphology of the albites here, they all show signs of hydrothermal metasomatism; (f-g) CGMs in different forms, with relation to the hydrothermal activities, note the CGM in close proximity to the smectite-illite mixed layer (I-S), which may indicate the migration of Ta-(Nb) with hydrothermal fluids; (h-i) Intergrowth of zircon, monazite and CGMs in the late stages. Mineral abbreviations: Cst- cassiterite; Ab- albite; Tan- tantalite; Col- columbite; Zrn- zircon; Ms- muscovite; Kfs- K-feldspar; I-S- illite-smectite mixed layer; Mnz- monazite.

by reducing volume and promoting rapid washout. Helium is used as the carrier gas and argon as the compensating gas to adjust the sensitivity of the stripping system during laser stripping, and the two gases are mixed via a T-junction before entering the ICP. Laser with a repetition rate of 10 Hz and energy density of 10 J/cm² was utilized during the analysis, and laser spot sizes ranged from 16 ~ 44 μm for fluid inclusion analyses. SILLS software was used to reduce the raw LA-ICP-MS data for fluid inclusion major and trace element calibrations (Guillong et al., 2008). To calibrate the analyses, the NIST SRM610 was used as an external standard, and the internal standard was set to NaCl equivalent wt.% concentrations, following the method described by Heinrich et al. (2003). Spectra with signals that coincided with Na and other cations were selectively processed to avoid interference from the host crystal. To adjust for the contributions of other chloride salts, the modeled Na amounts (in wt.% NaCl equiv.) were modified using the charge-balance technique, as outlined by Allan et al. (2005). Additional information about the analytical procedure can be found in Lan et al. (2018).

5. Results

5.1. Geochronology

The results obtained from the analysis of two cassiterite samples

from pegmatites in stage 2 using LA-ICP-MS can be found in the [Supplementary materials](#) and are outlined in Fig. 4. Forty spots of sample XS-2-6 were analyzed. These grains generally showed high U but low Th contents, with Th/U < 0.08. The Tera-Wasserburg U-Pb age was given from the lower intercept age of 147.4 ± 3.5 Ma, and the weighted mean ²⁰⁶Pb/²³⁸U age was obtained of 146.2 ± 2.5 Ma after ²⁰⁷Pb based correction (Fig. 4 a-b). And twenty-one spots of sample SHY21-05 were measured, the analyses take on a larger range of Th and U contents (0.003–3.5 ppm Th, 15.7–361 ppm U). The Tera-Wasserburg lower intercept analysis yielded an age of 147.7 ± 1.9 Ma, and the weighted mean ²⁰⁶Pb/²³⁸U age was 147.5 ± 2.2 Ma (Fig. 4c-d). These dating results obtained from the aforementioned suggest the Late Jurassic metallogenies.

5.2. Fluid inclusion study

5.2.1. Fluid inclusion petrography

Our study was focused on liquid-type, vapor-type and CO₂-type primary or pseudosecondary inclusions. Secondary inclusions typically form along healed microfractures within trails, and are thought to have formed long after the mineralization, were not studied in detail. Both liquid-type and vapor-type FIs consist of two phases and thus can be divided into LV- and VL-types pursuant to their vapor/liquid ratios. The

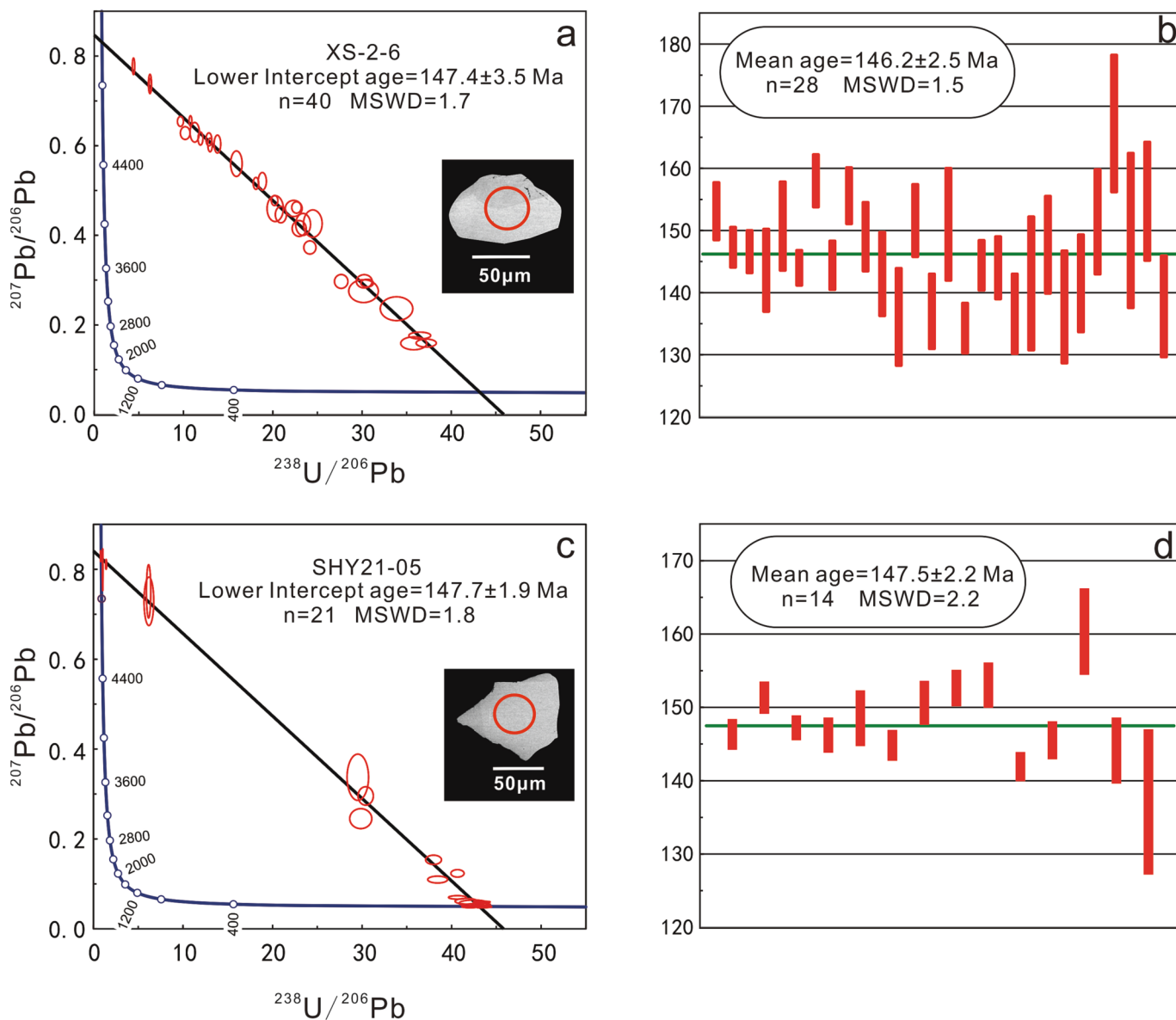


Fig. 4. Tera-Wasserburg U-Pb concordia plots and weighted mean ^{207}Pb corrected $^{206}\text{Pb}/^{238}\text{U}$ age diagrams for cassiterite from Shihuiyao deposit. (a-b) sample XS-2-6 and (c-d) sample SHY21-05.

LV-type FIs are liquid-rich, containing mostly 5 ~ 40 vol% vapor (Fig. 5a-d). They vary in shapes, ranging from irregular, oval, sub-rounded, to elongated, with diameters of 2 ~ 30 μm . When heated, they transform into a liquid state. Additionally, there is a subset of inclusions known as VL-type that have diameters ranging from 10 ~ 20 μm and contain 60 ~ 90 vol% vapor. Upon heating, they transform into a gaseous state. These inclusions can be found individually or in conjunction with LV-type FIs (Fig. 5-f) and might therefore be primary.

Solid-type FIs (S-type) are aqueous liquid-vapor-solid (L-V-S) multiphase inclusions (Fig. 5b, c). These S-type inclusions, primarily originating during the leucogranite stage (stage 2), exhibit sizes ranging from 10 ~ 20 μm and are characterized by liquid volumes of 50 ~ 60 vol % and vapor bubble volumes of 10 ~ 30 vol%, and daughter crystals, including sylvite, calcite, rhodochrosite, and anhydrite, are also present. The prismatic-shaped solids (<10 μm) exhibit a milky white and anisotropic appearance (Fig. 5c). Minor inclusions are also discernible in albite-quartz veins of stage 1.

CO₂-type FIs (C-type) are irregularly shaped to rounded, 10 ~ 20 μm in size. These inclusions usually consist of three phases at room

temperature (Fig. 5c), presenting as vapor CO₂ + liquid CO₂ + liquid H₂O. While some inclusions exhibit a two-phase state at room temperature, they undergo a transition to a three-phase state upon cooling. The CO₂ contents range from 35 ~ 60 vol%, occasionally up to 85 vol%. C-type inclusions occur in quartz phenocrysts (stage 2) as well as in quartz from quartz veins.

5.2.2. Raman spectroscopy analyses

To determine the vapor compositions of representative fluid inclusions, Raman spectroscopy was employed. The analysis indicated that while C-type inclusions were only found in stage 2, trace amounts of CO₂ were detected in all measurements (Fig. 6). Besides minor CO₂ contents, weak peaks of N₂ and high peaks of CH₄ were also found in FIs from stages 3 and 4 (Fig. 6c-d). The results suggest that the fluids responsible for ore formation can be categorized into two stages. The early stage consisted of H₂O-CO₂-NaCl, while the later stage was characterized by H₂O-CO₂-CH₄-NaCl ± N₂ system fluids. These observations provide valuable information regarding the evolution of hydrothermal fluids in the Shihuiyao mining area.

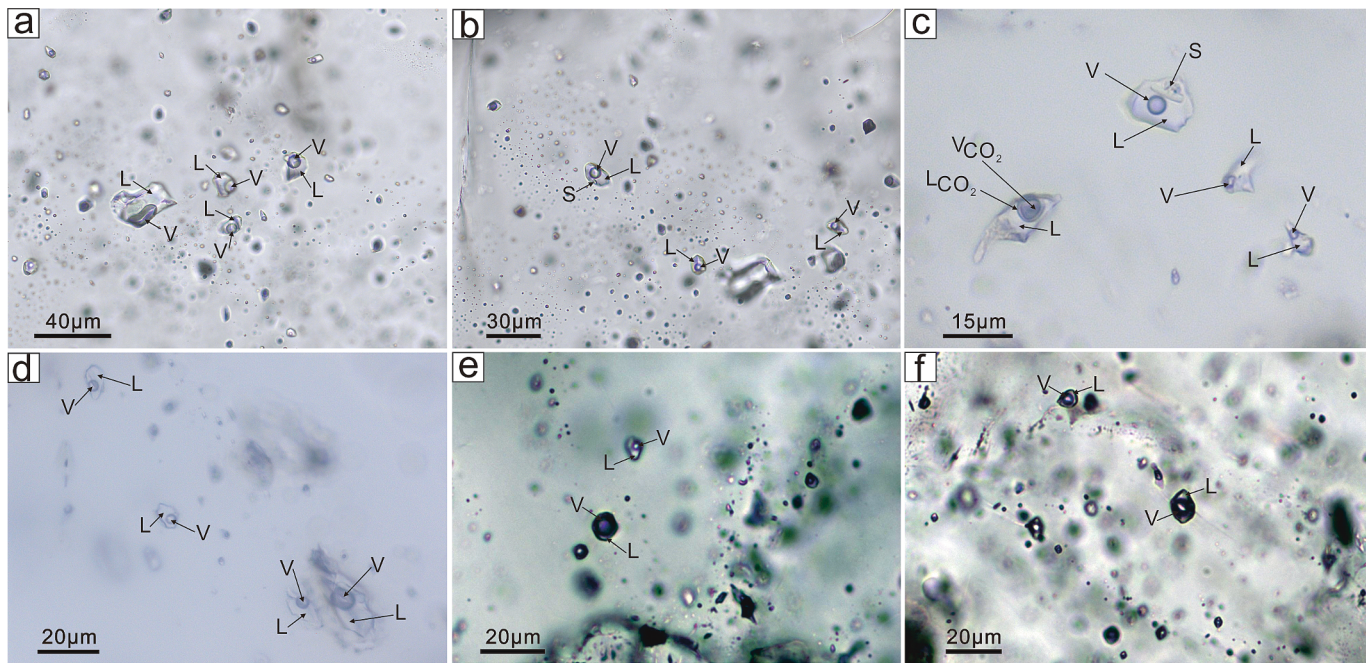


Fig. 5. Photomicrographs of FIs from the Shihuiyao Ta–Nb deposit. (a) LV-type FIs trapped in quartz (from stage 1); (b) S-type FIs coexists with LV-type FIs (from stage 1); (c) S-type FIs coexists with LV-type and C-type FIs (from stage 2); (d) Relatively large LV-type FIs in quartz (from stage 2); (e–f) LV-type FIs coexists with LV-type FIs (from stage 3–4). Abbreviations: L- liquid; V- vapor; S- solid.

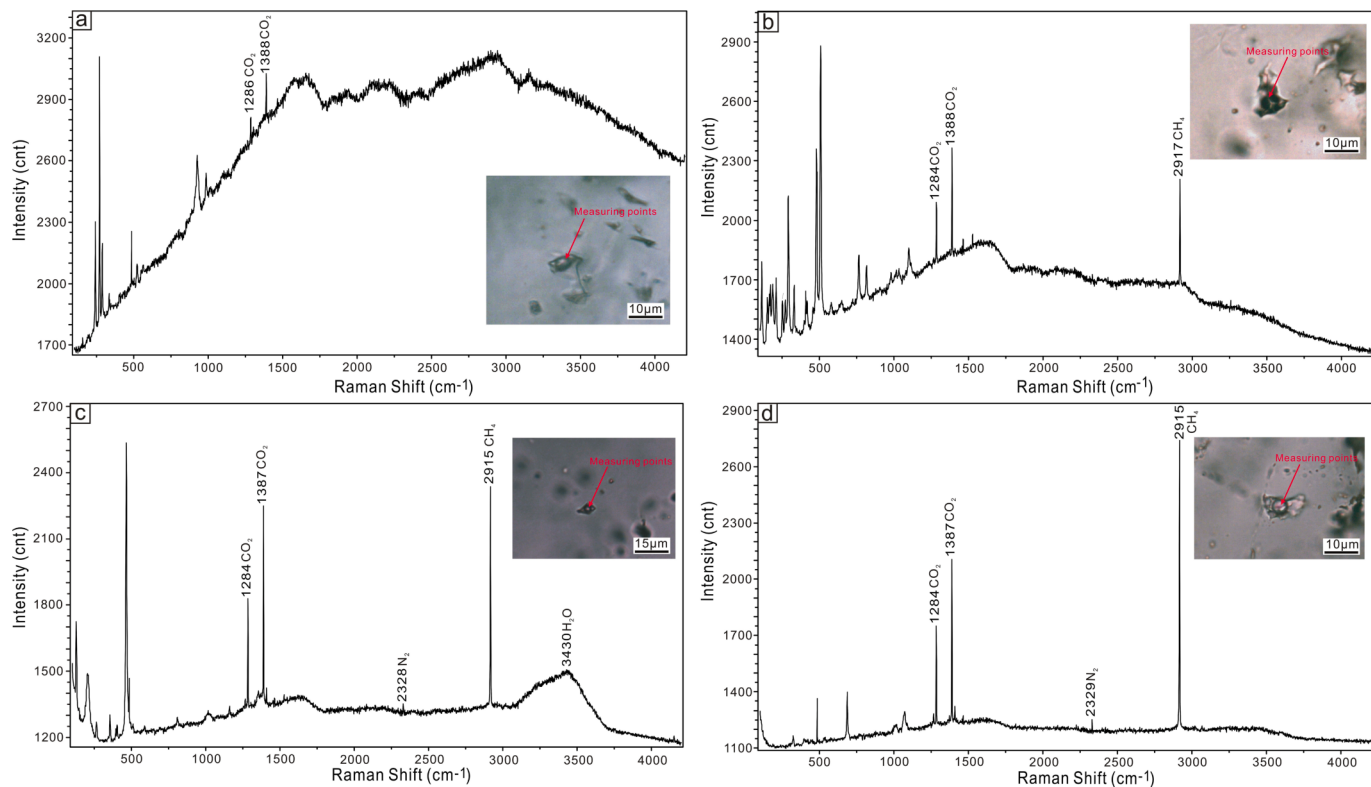


Fig. 6. Laser Raman spectra of FIs of the Shihuiyao deposit. (a) The vapor phase composition of LV-type FIs in quartz of stage 1; (b) The vapor phase composition of LV-type FIs in quartz of stage 2; (c) The vapor phase composition of LV-type FIs in amazonite of stage 3; (d) The vapor phase composition of LV-type FIs in fluorite of stage 4.

5.2.3. Microthermometry

Microthermometric measurements were conducted on 315 primary LV-type, 9 S-type and 12C-type inclusions hosted by different minerals during all mineralization stages (Table 1; Fig. 7). The specific

descriptions are as follows.

FIs in quartz of stage 1 are dominated by LV-type (Fig. 5a) with ice-melting temperatures from -11.2 to -0.8 °C and salinities of 1.06–15.09 wt% NaCl equiv. They generally homogenized to liquid at 264–397 °C,

Table 1

Fluid inclusions microthermometric data of the Shihuiyao Ta-Nb deposit.

Stage	Host mineral	Type	Num.	Size (μm)	Vapor (vol.%)	T _m -CO ₂ (°C) ^a	Th-CO ₂ (°C) ^b	T _d ^c or T _m clath (°C) ^d	T _m -ice (°C) ^e	Th (°C) ^f	Salinity (wt.% NaCl equiv.)	Bulk density (g/cm ³)	Estimated pressure (bar) ^g
1	Quartz	LV	97	2–30	25–80				−11.2 to −0.8	264–397	1.06–15.09	0.55–0.82	185.25–410.91
		B	3	10–20	30–40			182–395	−18 to −28	320–406	7.60–10.60	0.67–0.85	205.78–334.73
2	Quartz	LV	106	3–20	15–80				−8.8 to −1.5	213–370	2.00–8.82	0.58–0.91	163.12–368.85
		B	6	8–25	50–80			163–372	−22 to −33	241–393	5.33–6.37	0.78–0.86	213.27–340.99
		C	12	10–20	65–80	−62.3 to −56.6	12.3–29.5	0.7–3.4		255–337	4.62–4.80		210.24–277.85
3	Fluorite	LV	36	3–32	15–90				−10.2 to −0.3	164–315	1.91–6.59	0.75–0.93	114.01–283.86
		Quartz	22	2–20	10–25				−9.8 to −0.1	109–228	3.06–14.64	0.85–1.05	94.85–174.18
		Albite	17	3–15	10–20				−7.1 to −0.2	132–236	2.07–5.26	0.85–0.96	98.20–191.76
4	Fluorite	LV	25	5–40	10–25				−7.3 to −0.1	130–269	1.06–10.24	0.86–0.97	93.62–279.96
		Quartz	12	3–10	15–70				−9.2 to −0.5	119–166	10.19–12.94	0.98–1.03	133.69–179.29

^a CO₂ melting temperature.^b Temperature of homogenization to the liquid for CO₂.^c Solid dissociation temperature.^d Melting temperature of clathrate.^e Final ice melting temperature.^f Homogenization temperature.^g The trapping pressure and Th correction was estimated by using the salinity of fluid inclusions, homogenization temperature (Th), and the temperature of mineral formation defined by mineral paragenesis (Roedder, 1984).

with a peak of 280–340 °C, and in the minor S-type inclusions (Fig. 5b), the melting temperatures of daughter crystals show a wide range from 182 °C to 395 °C, suggesting salinities of 7.60–10.60 wt% NaCl equiv. The homogenization temperatures of these inclusions are between 320 and 406 °C (Fig. 7a, b). The similarity in homogenization temperatures of both types of fluid inclusions, as well as their association with the surrounding space, suggests the boiling of fluids occurred at the early ore stage. The calculated bulk densities of the LV-type and S-type FIs in stage 1 are 0.55–0.82 and 0.67–0.85 g/cm³, respectively.

Three types of FIs could be identified in quartz during stage 2, mainly LV-type, with a small amount of S-type and C-type FIs (Fig. 5c, d, Table 1). Their similar homogenization temperatures indicate trapping during fluid boiling. The LV-type FIs yielded T_m-ice of −8.8 to −1.5 °C and salinities of 2.00 to 8.82 wt% NaCl equiv. The T_m-ice of the S-type FIs range from −22 to −33 °C, and the daughter crystals dissolved at temperatures between 163 and 372 °C, corresponding to salinities between 5.33 and 6.37 wt% NaCl equiv. In the C-type FIs, on warming after freezing, the solid CO₂ phase melted at −62.3 to −56.6 °C, slightly below the triple point of pure CO₂ (−56.6 °C), indicating a few mixing with other vapor phase components, such as N₂ and CH₄ as demonstrated by Raman spectrum (Fig. 6b), with further homogenization to liquid at +12.3 to +29.5 °C (Table 1). Clathrate melting in the C-type FIs occurs at +0.7 to +3.4 °C which, in the NaCl–CO₂–H₂O system, indicates salinities of 4.62–4.80 wt% NaCl equiv. In general, all the homogenization temperatures of FIs in stage 2 range from 213 to 393 °C, peaking at 260–320 °C (Fig. 7c, d). Salinities calculated from these FIs range from 2.00 to 8.82 wt% NaCl equiv., with the estimated bulk densities are 0.58 ~ 0.91 g/cm³ (Table 1).

Only LV-type FIs were tested in stages 3 and 4 (Fig. 5e, f). FIs in fluorite of stage 3 yielded homogenization temperatures of 164–315 °C and salinities of 1.91–6.59 wt% NaCl equiv. (Table 1; Fig. 7e, f). Similar lower Th (109–228 and 132–236 °C, respectively) were recorded by FIs in quartz and albite of stage 3, with variable salinities ranging from 3.06 to 14.64 and 2.07–5.26 wt% NaCl equiv., respectively. The FIs in stage 3

were homogenized to liquid or vapor at 109 to 315 °C, concentrating in the range of 160–240 °C. Bulk densities of the FIs range from 0.75 to 1.05 g/cm³ (Table 1). The FIs in fluorite and quartz of stage 4 yielded similar Th (130–169 and 119–166 °C, respectively) but different salinities (1.06–10.24 and 10.19–12.94 wt% NaCl equiv., respectively) (Fig. 7g, h). The total homogenization temperatures of these fluid inclusions in stage 4 range within 119–169 °C, with a peak of 140–160 °C. Bulk densities of these inclusions were calculated between 0.86 and 1.03 g/cm³.

5.2.4. Elemental compositions of fluid inclusions

Fourteen individual fluid inclusions from four LV-type FIAs in quartz were subjected to microanalysis using LA-ICP-MS. The complete dataset for each fluid inclusion, comprising all selected elements and ratios, are outlined in Table 2. Almost all the inclusions contain Li, Na, Mg, Al, Cl, K, Ca abundantly (mostly more than 10⁴ ppm) and Rb, Sr, Sn, Cs, W in relatively small contents (mostly less than 10³ ppm). Specifically, the concentrations of Ca, Na and K range from 8055 to 48421 ppm, 4433 to 139673 ppm and 5134 to 42643 ppm, respectively. The mean concentrations of Cs, Rb, Sr and Sn in the deposit are 176, 474, 91 and 54 ppm, respectively. Despite tantalum and niobium being the most economically significant in the deposit, they were not detected in all of the fluid inclusions.

6. Discussion

6.1. Late Jurassic mineralization of Shihuiyao deposit

Several investigations have been conducted to establish the diagenetic and metallogenic timeframes of the Shihuiyao deposit. Duan et al. (2021) identified six intrusive plutons in the ore field, generating monazite U-Pb ages of ca. 145 Ma. Zhou et al. (2022) also reported the monazite U-Pb ages of 150.2 ± 0.6 Ma and 147.0 ± 1.7 Ma for the porphyritic granite and leucogranite, respectively, demonstrating the

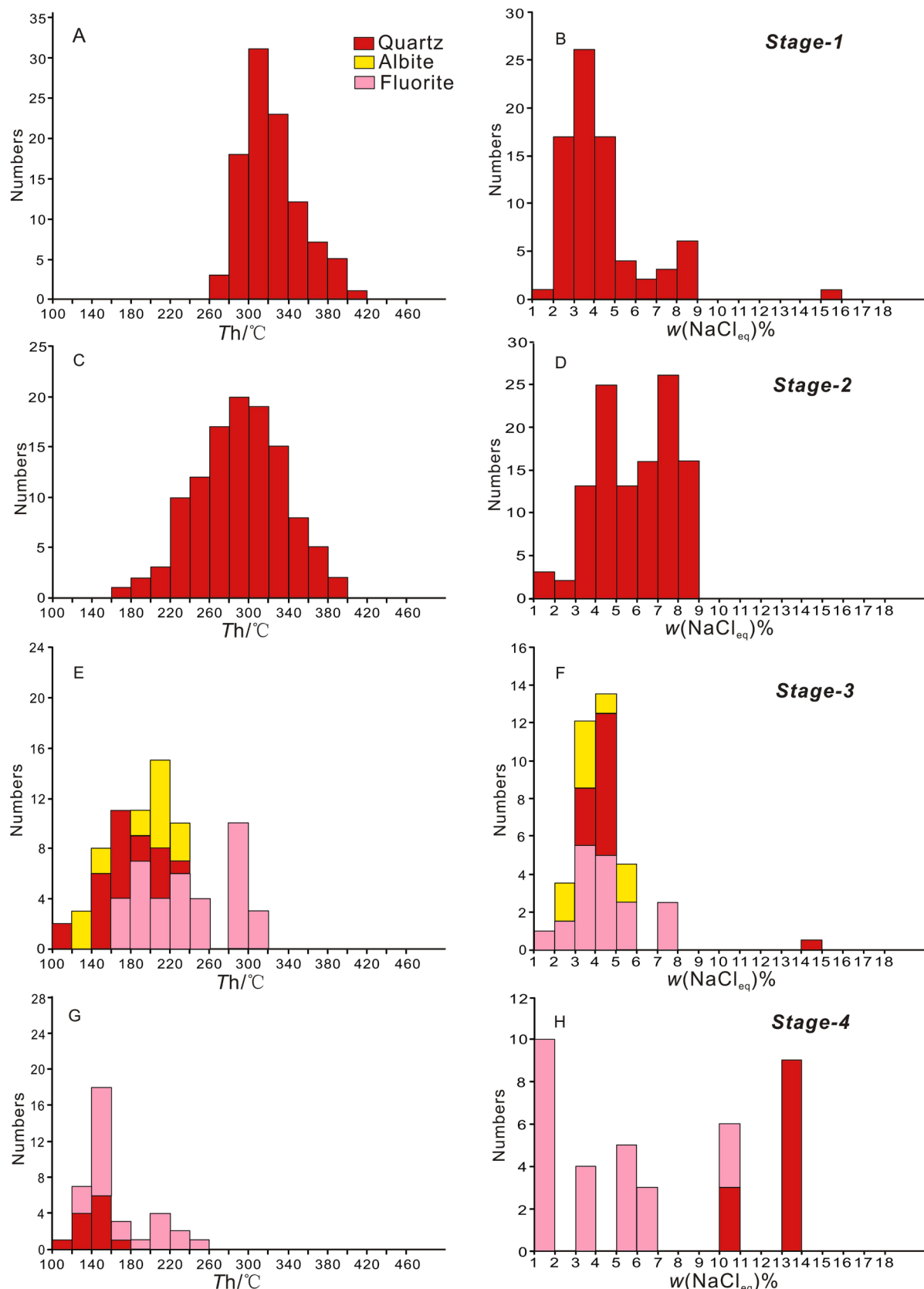


Fig. 7. Frequency histogram of homogenization temperatures and salinities for the FIs in the Shihuiyao deposit.

Table 2

Elemental compositions and selected elemental ratios of all analyzed fluid inclusions.

Sample	Lithology	Th/°C	Li μg/g	Na μg/g	Mg μg/g	Al μg/g	Cl μg/g	K μg/g	Ca μg/g	Cu μg/g	Zn μg/g
XS-3-6	PG	349	<37.6	13,648	875	9085	<23792	5134	<34065	928	1227
XS-5-5-A1(1)	LGa	284	992	25,786	3010	48,549	<36689	30,472	<65062	901	5757
XS-5-5-A1(2)	LGa	324	1134	27,616	8793	65,205	37,997	27,658	<68846	2095	27,152
XS-5-5-A1(3)	LGa	307	11,113	139,673	6334	99,677	<194682	42,643	<343590	<2328.7	10,589
XS-5-5-A3(1)	LGa	270	<53.8	22,799	3220	7240	27,301	6340	48,421	1117	4590
XS-5-5-A3(2)	LGa	330	181.45	25,904	606	2718	36,161	8416	<66066	942	2800
XS-1-26-A2(1)	LGg	229	<10.4	4433	30	68,663	<6852	29,929	<9691	97	275
XS-1-26-A2(2)	LGg	256	3528	40,099	2110	54,269	68,340	28,375	<101489	1659	88,664
XS-1-26-A2(3)	LGg	292	<24	9140	851	34,942	<15104	17,378	<22440	<144.4	395
XS-1-26-A2(4)	LGg	277	218	12,737	172	17,043	21,336	13,720	<32184	709	819
XS-1-26-A3(1)	LGg	284	52	14,946	57	<105.9	<20227	<2965	<22198	<151.3	74
XS-1-26-A3(2)	LGg	299	21	15,657	108	22,850	9833	<192	8055	115	3004
XS-1-26-A3(3)	LGg	261	NA	15,657	NA	NA	NA	NA	NA	869	NA
XS-1-26-A3(4)	LGg	285	NA	15,657	NA	NA	NA	NA	NA	NA	NA
Sample	Rb	Sr	Sn	Cs	W	NK	Sn/NK	Cs/NK	Rb/NK	Cs/Na*1000	Sn/Na*1000
	μg/g	μg/g	μg/g	μg/g							
XS-3-6	110	29	22	5	<12.3	18,782	0.0012	0.0002	0.0059	0.33	1.61
XS-5-5-A1(1)	1207	190	45	430	85	56,258	0.0008	0.0076	0.0215	16.68	1.74
XS-5-5-A1(2)	674	321	163	411	130	55,274	0.0030	0.0074	0.0122	14.89	5.92
XS-5-5-A1(3)	164	270	233	348	<148.8	182,315	0.0013	0.0019	0.0009	2.49	1.67
XS-5-5-A3(1)	43	252	35	5	<19.6	29,140	0.0012	0.0002	0.0015	0.21	1.52
XS-5-5-A3(2)	110	39	35	43	<9.4	34,320	0.0010	0.0013	0.0032	1.66	1.36
XS-1-26-A2(1)	1296	2	33	72	3	34,362	0.0010	0.0021	0.0377	16.14	7.50
XS-1-26-A2(2)	700	104	67	572	62	68,474	0.0010	0.0084	0.0102	14.26	1.68
XS-1-26-A2(3)	452	48	96	2	9	26,518	0.0036	0.0001	0.0170	0.19	10.50
XS-1-26-A2(4)	544	<4.7	54	403	<11.5	26,457	0.0020	0.0152	0.0206	31.66	4.21
XS-1-26-A3(1)	65	4	17	66	<8.2	14,946	0.0012	0.0044	0.0044	4.41	1.16
XS-1-26-A3(2)	9	6	NA	3	3	15,657	NA	0.0002	0.0006	0.16	NA
XS-1-26-A3(3)	NA	NA	NA	NA	NA	15,657	NA	NA	NA	NA	NA
XS-1-26-A3(4)	NA	NA	28	97	40	15,657	0.0018	0.0062	NA	6.19	1.79

Note: Values below detection limits or anomalous results were excluded from the calculation; NK = Na + K; NA = Not Applicable.

presence of Late Jurassic magmatism in the Shihuiyao. Moreover, muscovite ^{40}Ar - ^{39}Ar dating from pegmatite and greisenized leucogranite give plateau ages of 146.4 ± 1.0 Ma and 144.7 ± 1.1 Ma, respectively (Sun et al., 2015), comparable to those of Zhou et al. (2022) (146.3 ± 1.1 Ma from leucogranite, 145.6 ± 1.0 Ma from quartz-mica vein,

respectively). On the other hand, direct dating of ore minerals is the most effective way to determine the metallogenetic age. Here we acquired two ^{206}Pb - ^{238}U ages of 147.4 ± 3.5 Ma and 147.7 ± 1.9 Ma, respectively, obtained from the cassiterite samples from stage 2, which are consistent with ages determined by columbite U-Pb ages (146.7 ± 4.7

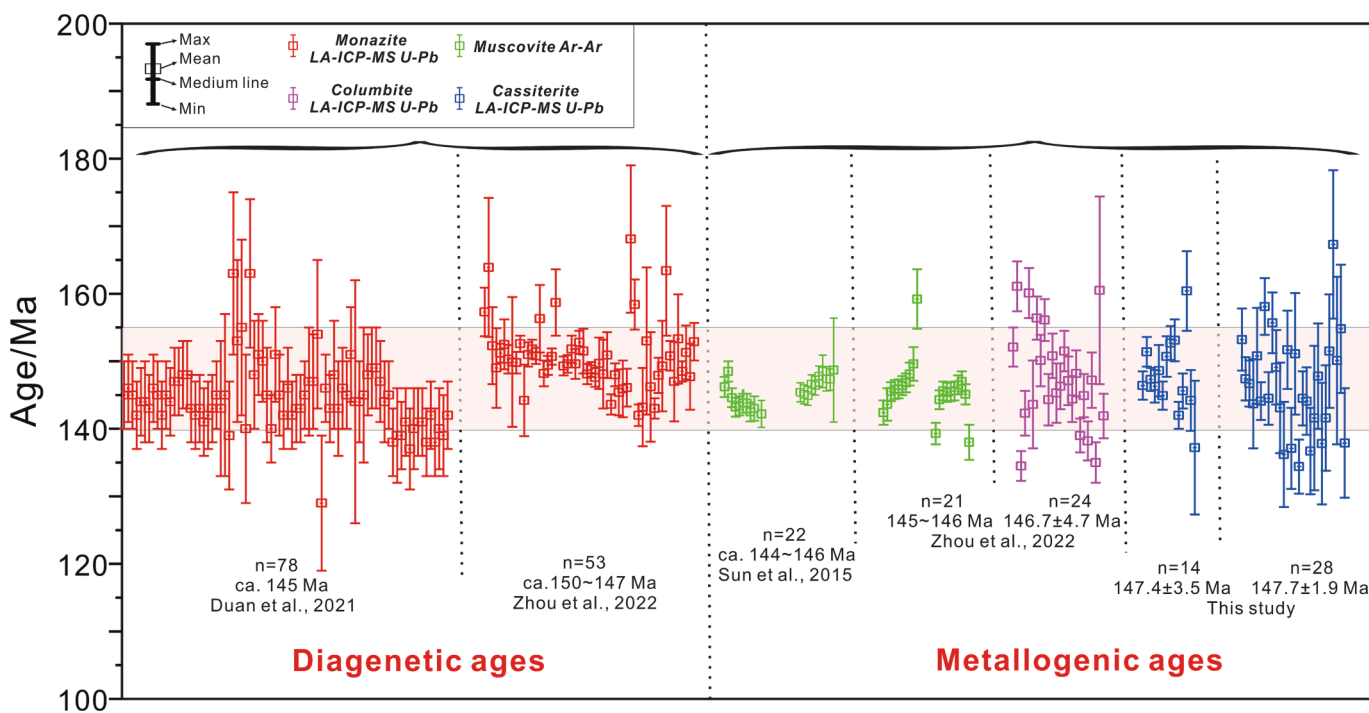


Fig. 8. Geochronology framework of the Shihuiyao deposit, within both magmatism and metallogenies ages. Data from Sun et al., 2015; Duan et al., 2021; Zhou et al., 2022 and this study.

Ma, Zhou et al., 2022). The consistency of these ore mineral dating results demonstrates the intimate relationship between the Late Jurassic granitic magmatism and contemporaneous Ta-Nb mineralization in the Shihuiyao deposit (Fig. 8).

Rare metal deposits in the SGXR that formed during the late Mesozoic exhibit relatively low initial ($^{87}\text{Sr}/^{86}\text{Sr}$)_i, positive $\varepsilon_{\text{Nd}}(\text{t})$ and $\varepsilon_{\text{Hf}}(\text{t})$ values and young two-stage model ages (e.g., Duan et al., 2021; Su et al., 2021; Wu et al., 2021; Zhou et al., 2012), indicating the source of ore-bearing rocks is primarily derived from the Neoproterozoic juvenile crustal materials that similar to the depleted mantle. Moreover, the isotopic analysis of $\delta^{34}\text{S}$ and He-Ar in the ore minerals similarly revealed strong mantle involvement during mineralization process in the SGXR (Zhou and Mao, 2022; Zhou et al., in review). During the Late Jurassic, the SGXR was in a transitional stage between two giant tectonic systems, i.e., Mongol-Okhotsk Ocean domain and Paleo-Pacific domain, despite the ongoing controversy surrounding the SGXR's geodynamic background during this period (Shao et al., 2010; Wilde and Zhou, 2015; Li et al., 2017a; Li et al., 2017b; Li et al., 2017c; Wang et al., 2015; Wang et al., 2022), the NNE-oriented outcrop rocks in the Shihuiyao mining area and the NEE-trending Mongolian-Okhotsk orogenic belt stand out as distinct features (Ouyang et al., 2015; Wu et al., 2021). We therefore believe that the deep geodynamics of the mineralized granite in the Shihuiyao deposit was caused by the low-angle subduction of the Paleo-Pacific Plate beneath the Eurasian Plate, coinciding with the northeast Asia continental margin's sliding event from low to high latitude (Xu et al., 2019). In the oblique extended subduction setting, the material of the asthenosphere rose, causing the Neoproterozoic crust to partially melt. With the long-term evolution, the magmas finally ascend and invade under the background of Mesozoic tectonic activation, forming the Shihuiyao and the other rare metal deposits in the SGXR (Ouyang et al., 2015; Mao et al., 2019; Chen et al., 2022).

6.2. Chemical quenching in low pressure and shallow mineralization environment

Fluid entrapment pressure can be estimated by studying FIs formed in immiscible or boiling systems (e.g., coexisting LV-type or VL-type and S-type inclusions with identical T_h) (Brown and Hagemann, 1995). In such systems, T_h is equal to the trapping temperature upon boiling, obviating the need for pressure correction to derive the trapping temperature (Roedder and Bodnar, 1980). As mentioned above, boiling or immiscibility has been observed during both stages 1 and 2 stages, allowing estimation of the trapping pressures of immiscible LV-type and S-type fluid inclusion assemblages using T_h and salinity values and correlations established by Driesner and Heinrich (2007). The obtained results indicate that the estimated fluid inclusion trapping pressures range from 185 to 410 bars for stage 1 and 163–368 bars for stage 2, assuming an overlying rock density of 2.5 g/cm³, corresponding to depths of 0.7–1.5 km and 0.6–1.4 km, respectively, which reveals a marked discrepancy in intrusion pressure (depth) between the particular Shihuiyao and other analogous Ta-Nb-(Sn) deposits (Fig. 9), which showed observably mineralized under high-pressure conditions (Nakano and Urabe, 1989; Černý et al., 2005). The Nb-Ta mineralization is often found in granitic-pegmatites, such as Yashan, Renli, etc., primarily at pressures ranging from 200 to 400 MPa (Černý et al., 2005; London, 2008). The high-pressure in the deep is typically conducive to the accumulation of volatile elements (e.g., P, Li, F, B), which play a vital role in the formation and mineralization of rare-metal granites. In contrast, shallow-level intrusions, such as Shihuiyao, may have distinctive genetic mechanisms due to their unique geological settings.

Depth of magma intrusion is contingent upon several factors, including magma viscosity, the time the ore-forming fluid was released, geothermal gradient, etc., the viscosity of magma is intimately linked to the magma differentiation process. Magmas that have experienced extensive evolution at depth are more prone to the process of volatile-rich melt/fluid fractionation, which in turn can lead to an increase in

residual magma viscosity, a deceleration in intrusion rate, and ultimately, the emplacement of the magma at a deeper depth (Qin et al., 2021). Hence, the origin of high-fractionated leucogranites, that are shallowly intruded in the mining area, could be explained by the fractionation process occurring at shallow depths, where the exsolution of volatiles in the shallow magma chamber causes the melts to finally settle at a depth of <2 km (Fig. 9). The shallow intrusive fractionation or a shorter time of separation between the ore-forming fluids and residual melts, which resulted in the omission of transport time and subsequently retarded the decrease in temperature of the ore-forming fluids. As a result, the primary mineralization temperature of the Shihuiyao deposit was found to be higher than that of other Ta-Nb deposits (Fig. 11), and the physicochemical evolution of fluids within metallogenic intrusions is highly dependent on the depth of intrusion, as stated by Audébat (2019), fluids that exsolve from high-pressure condition (deeper depth) are in the single-phase state with intermediate densities and lower salinities, varied from those in shallow level intrusions, which show relatively high-salinity characteristics (Fig. 11).

More significantly, the low-pressure and shallow-level metallogenic environment is more conducive to the chemical quenching process, which further supported by the occurrence of K-feldspar as a pure composition and in a branchlike form but not as perthite (Zhou et al., 2022; Xie et al., 2019). Chemical quenching involves the dissipation or removal of fluxed components through crystallization, diffusion, or vapor-phase loss, resulting in the crystallization of CGMs (e.g., London, 2008; Akinfiev et al., 2020), which accompanied by the instability of fluoride complex and the neutralization of acid fluorine complex.

The FLINCOR program developed by Brown and Lamb (1989) was utilized to estimate the entrapment pressures for C-type inclusion fluids. Additionally, the equations provided by Bowers and Helgeson (1983) for a CO₂-H₂O-NaCl system were applied. The estimated trapping pressure is 210–277 bars at temperatures of 255–337 °C (Table 1). Notably, this pressure estimation agrees with Bowers and Helgeson's (1983) conclusion that when subjected to low pressures (<100 MPa), a H₂O-CO₂ fluid with a salinity of 6 wt% NaCl equiv. displays immiscible behavior, separating into a brine and a low-salinity CO₂-bearing vapor. However, at pressures exceeding 100 MPa, the same fluid produces low-salinity CO₂-H₂O mixtures without the presence of brines due to the immiscibility between the two phases. Besides, the T_h values of FIs derived from uniform fluids exhibit the minimum range of fluid temperatures, suggesting the pressures determined for non-boiling assemblages signify minimum values (Roedder, 1984). LV-type inclusions for stages 3–4 yielded T_h ranging from 109 to 315 °C and pressures ranging from 93 to 283 bars (Steele-MacInnis et al., 2012), representing only their minimum trapping pressures (Roedder and Bodnar, 1980). Fluids with low pressures indicate that the Shihuiyao deposit was formed in a shallow environment under mostly hydrostatic conditions, during the early stages. The ore-forming process across this deposit involved the sequential formation of lithostatic and hydrostatic pressures, as evidenced by the maximum and minimum pressures, respectively (e.g., Rajabpour et al., 2018).

6.3. Fluid evolution and ore-forming mechanisms

Understanding the ore-forming processes is crucial to unraveling the genesis of rare metal deposits. The processes that result in the precipitation of ore minerals are primarily governed by immiscibility, fluid mixing, cooling, and fluid-rock interaction (Wilkinson, 2001; Vasyukova and Williams-Jones, 2014; Rottier et al., 2016). In this regard, we consider that fluid inclusions can provide powerful insights into the mineral genesis mechanisms in the Shihuiyao deposits.

Characteristics of fluid evolution at the Shihuiyao deposit are summarized as follows. Magma degassing would occur during crystallization at shallow depths (e.g., Samson et al., 2008). The high degree of differentiation during the magmatic stage, intense tantalum-rich hydrous silicate fluid metasomatism, rapid magma quenching and fluid boiling

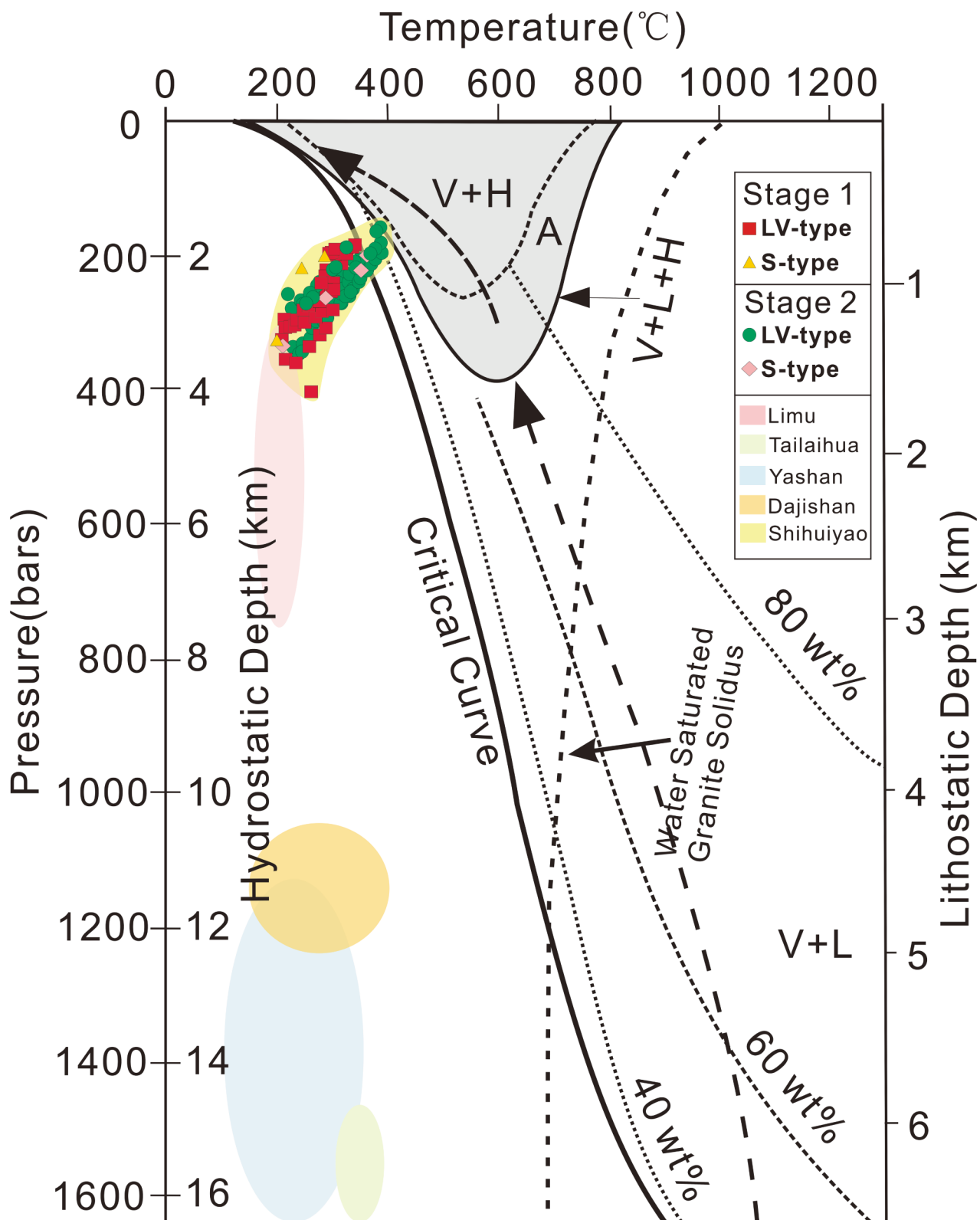


Fig. 9. Phase relations in the NaCl-H₂O system modified from Muntean and Einaudi (2001) and Mernagh and Mavrogenes (2019). Depths assuming a 1 g/cm³ hydrostatic load and a 2.5 g/cm³ lithostatic load are also shown. Isopleths of NaCl in liquid in the twophase vapor + liquid field are shown by the short dashed lines. The shaded region depicts the vapor + halite field. Dashed curve A is the liquid saturation curve for the NaCl-KCl-H₂O system where Na/K ratios in the solution are fixed by equilibration with albite and K-feldspar at the indicated temperatures. The heavy dotted line is the H₂O-saturated granite solidus from Audétat and Simon (2012). The heavy dashed arrows show the proposed fluid path based on the fluid inclusion data. This figure highlights the characteristics of shallow emplacement of Shihuiyao Ta-Nb deposit. Abbreviations: V- vapor, L- liquid, H- halite. Data source: Limu from Liang et al., 2012; Tailaihua from Sun, 2013; Yashan from Li et al., 2017b; Dajishan from Xi et al., 2008.

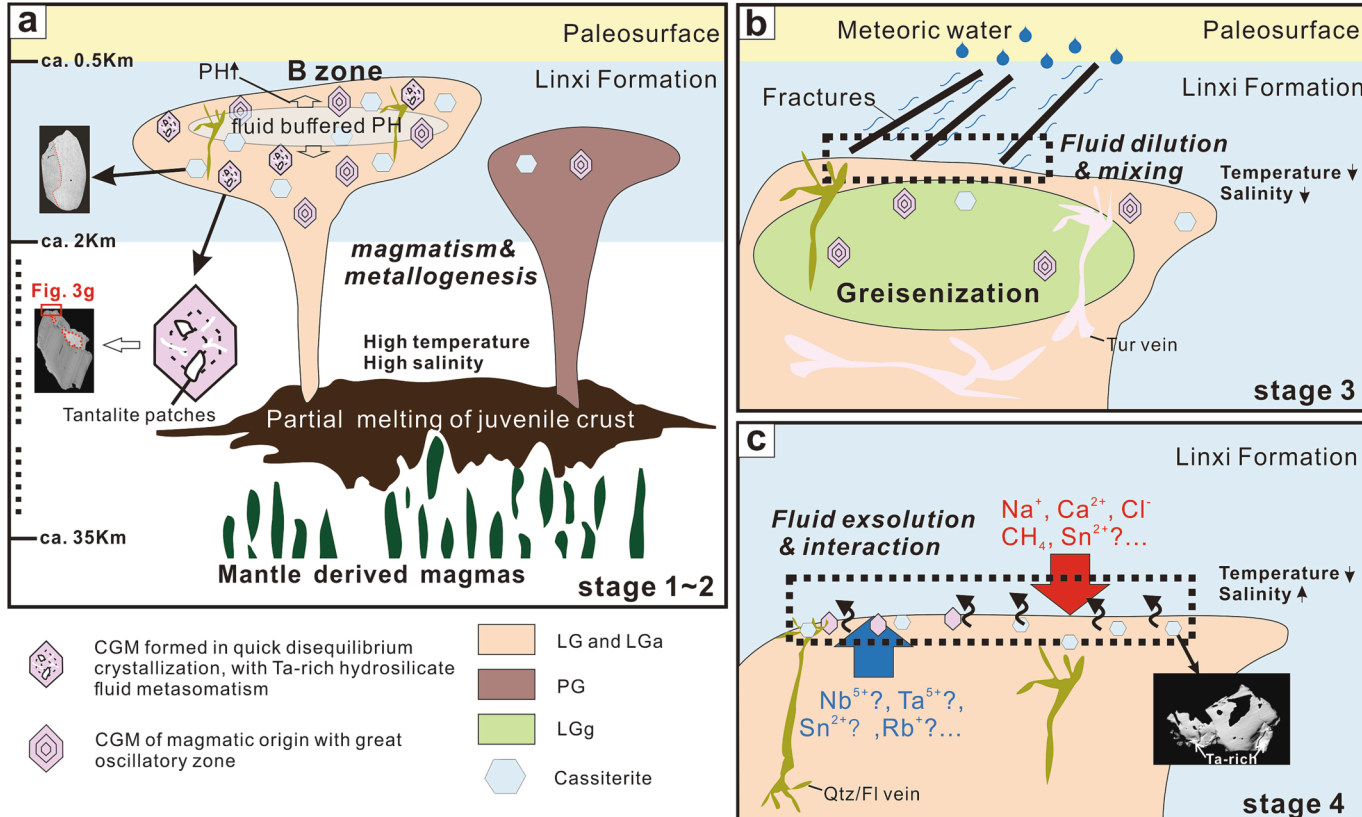
collectively facilitate the abundant crystallization of CGMs. Mineralized fluids during this stage exhibit characteristics of high temperature and high salinity (Fig. 10a). Moving on to stage 3, although the salinity range is broad (1.9–14.6 wt% NaCl equiv.), it mainly aggregates between 3.1 and 5.7 wt% NaCl equiv.. Generally, as the temperature decreases, the total density of the fluid increases, while the salinity and contents of CO₂ and other volatiles decrease, which can be attributed to the mixing with meteoric water (e.g., Wilkinson, 2001, Fig. 10b). Among magmatic-hydrothermal deposits, mineral precipitation is influenced by destabilizing processes of metal complexes transported by fluids, as noted by Zajacz et al. (2008). The evidence of fluid boiling assemblages was observed during stages 1–2. Boiling of the fluid caused continuous escape of gaseous H₂O and volatile H₂S, CO₂, HCl, and HF, resulting in an increase in pH and a decrease in temperature within the fluid (i.e., $2\text{H}^+ + \text{CO}_3^{2-} \rightarrow \text{H}_2\text{O} + \text{CO}_2$), along with the breakdown of metal complexes within the fluid (Phillips and Evans, 2004; Runyon et al., 2017). The crystallization temperatures of Rb-rich micas were estimated to be no higher than 300 ~ 400 °C, which implies that the mineralization most likely occurred during the hydrothermal evolutionary stage of the pegmatite system (Pekov and Kononkova, 2010), and this is consistent with the FI microthermometric results indicating mineralization concentrated at 260–400 °C (Fig. 7). Experimental results (Linnen and Cuney, 2005) conducted in peraluminous melt also show that the solubility of Nb and Ta decreases by several orders of magnitude with the decrease in temperature from ~ 500 ppm Nb and ~ 2500 ppm Ta at 800 °C to 56 ppm Nb and 300 ppm Ta at 550 °C. In addition, as the pH goes up, fluorite precipitates, and the activity of HF reduces, which in turn facilitates the deposition of both niobium and tantalum (Timofeev et al., 2015). Fluid boiling thus interpreted as a major mechanism for Ta-

Nb mineralization at Shihuiyao. And during stage 3, a considerable decrease in temperature occurs in the hydrothermal fluid, resulting in a reduction of the solubility of mineralized elements (Nb, Ta). This phenomenon triggers the instability of these elements and enables their continued precipitation and deposition from the hydrothermal fluid, but it should be noted that large-scale mineralization does not occur during this stage, as most of the CGMs have been crystallized in the magmatic phase.

However, salinity is much higher (10.19–12.94 wt% NaCl equiv.) for FIs in quartz of stage 4 trapped at lower temperatures (119–166 °C) (Table 1). This is presumably due to the sudden increase in salt contents as a result of mixing with external fluids (Fig. 11) (Mangas and Arribas, 1987). Furthermore, a large proportion of FIs with significant CH₄ ± N₂ in stages 3–4 (Fig. 6) also supports the possible contribution of carbonic fluid from the country rocks (e.g., Mulja and Williams-Jones, 2018). The intense water–rock interaction between the mineralized fluids and the surrounding rocks may have enabled the migration of specific elements like Sn, which were already enriched in the strata, into the mineralized fluids, and may have caused the precipitation of cassiterites, which exhibits prominent hydrothermal alteration features, with Ta-rich components being observed to precipitate even in the margin parts (Fig. 10c). Additionally, some of the mineralized elements (e.g., Sn, Nb, Ta) could have been reactivated during this latest stage, resulting in the formation of a scarce amount of ore minerals.

6.4. The potential of tin mineralization

The SGXR has been recognized as a major multi-metal mineralization province in northern China, and considerable effort has been invested in



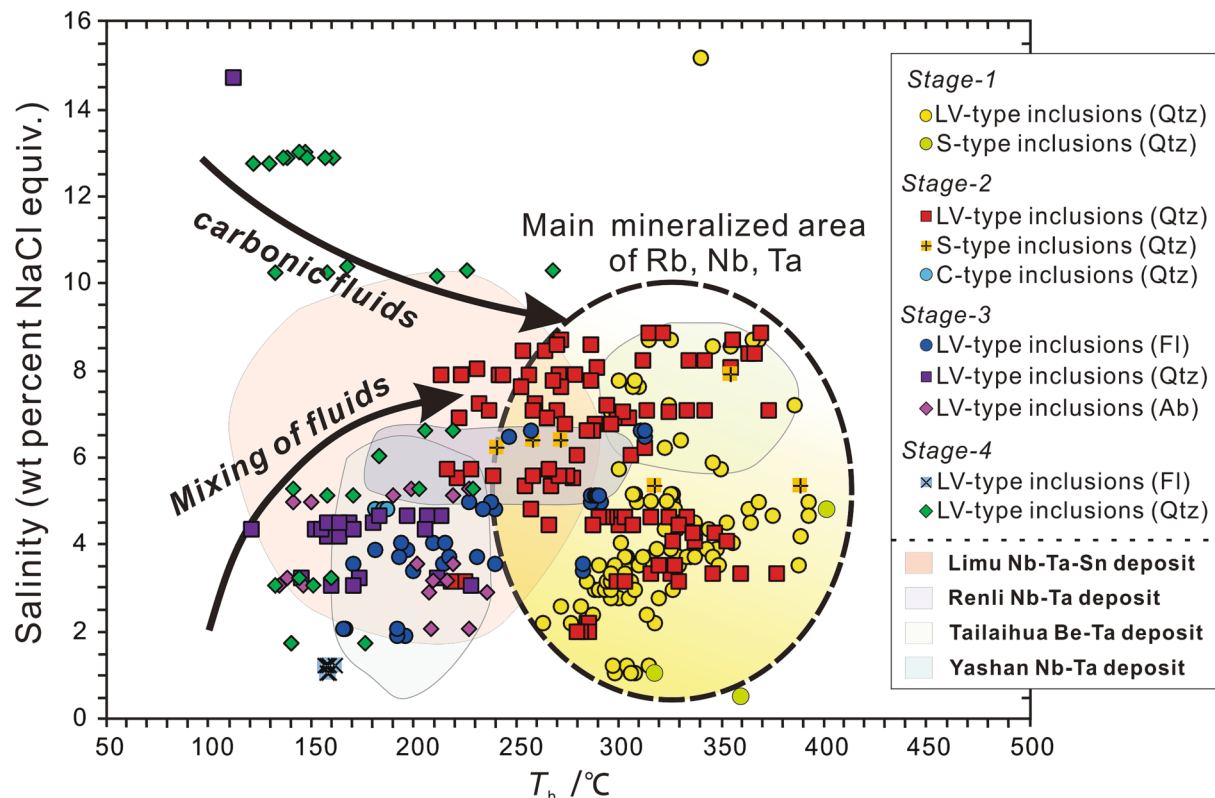


Fig. 11. Inclusion homogenization temperature (T_h) and salinity binary diagram to illustrate the characteristics of the main ore-forming fluids and the late external fluid mixing process. It is worth noting that during the main ore-forming stage (stage 1 and 2), the homogenization temperature of the Shihuiyao deposit is markedly higher than that of other Ta-Nb deposits, which may provide favorable conditions for chemical quenching to occur. Moreover, the Shihuiyao exhibits a distinct late-stage feature of high salinity fluid influx. Data source: Limu after Liang et al., 2012; Renli after Li et al., 2019; Tailaihua after Sun, 2013; Yashan after Li et al., 2017b.

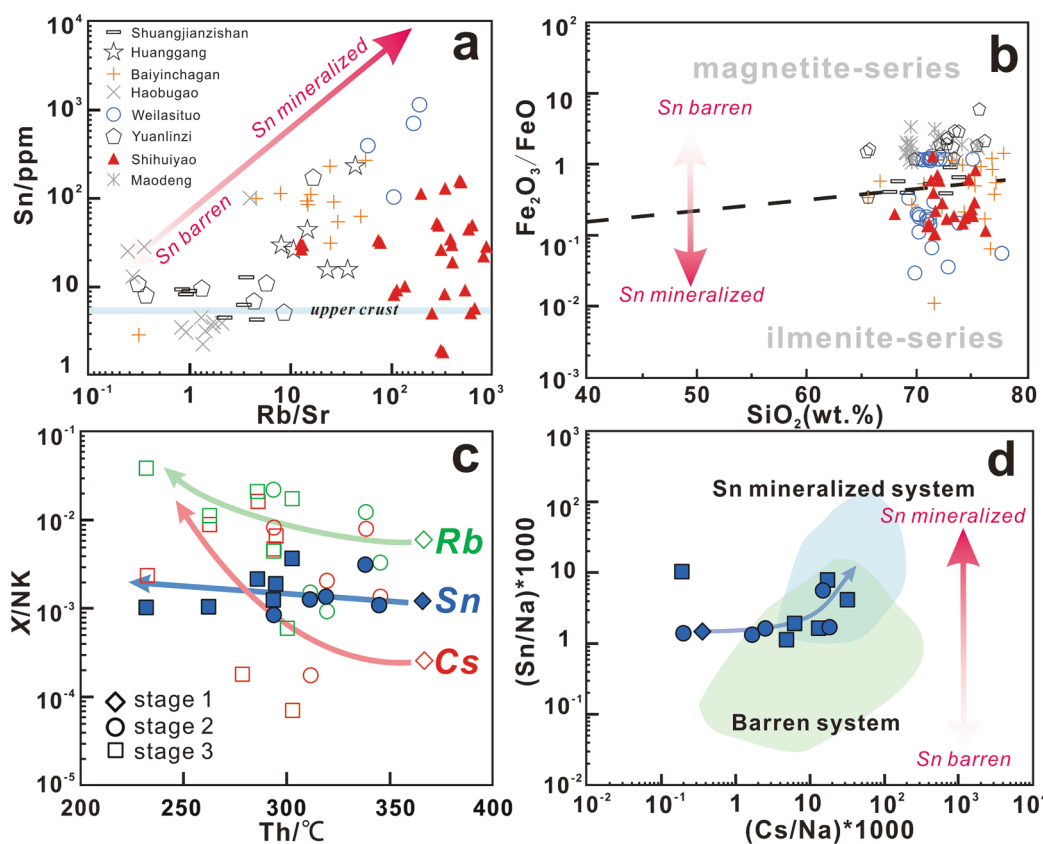


Fig. 12. Some geochemical diagrams are used to assess the characteristics of ore-bearing bodies (a-b) and fluids (c-d). Rb/Sr ratios vs Sn concentrations (a) and mass percentage of SiO_2 vs $\text{Fe}_2\text{O}_3/\text{FeO}$ ratios (b) to evaluate the fractionation and Rodex conditions, respectively; homogenization temperature (T_h) vs mass ratios $X/(\text{Na} + \text{K})$ (c) and sodium normalized metal abundance in fluids (d) to evaluate tin mineralization potential. Data source: Zhou and Mao, 2022; Chen et al., 2022; Zhou et al., 2022; Duan et al., 2021; Zhao et al., 2022a; Hu et al., 2020.

exploring Sn polymetallic deposits (e.g., Mao et al., 2019; Zhou and Mao, 2022) or Pb-Zn-Ag deposits (e.g., Ouyang et al., 2014; Zhai et al., 2019a; Zhai et al., 2019b; Shu et al., 2017). However, the possibility of tin mineralization in the Shihuiyao deposit, which is a relatively uncommon Ta-Nb mineralization in this belt, remains an unresolved yet relevant question. Cassiterites are rarely found in porphyritic granite, but can be easily identified and observed in other types of rocks, which inspired the speculation of Sn potential in unexplored parts of the system. Sn concentrations in Shihuiyao granites are varying from the barren tin mineralized granites in the SGXR but similar to those in superlarge-large deposits (Fig. 12a). In addition, most primary tin mineralization is spatially, temporally, and chemically associated with reduced, fractionated, and volatile-rich tin granites (Wolf et al., 2018; Lehmann, 1990, 2021). Shihuiyao granites exhibits high degree of fractionation and reduced characteristics (Fig. 12a, b), falling within the range of the ilmenite-series (Ishihara, 1981), and the widespread fluorites and minor amounts of tourmalines in the mining area suggest the initial characteristics of magma rich in volatiles, indicating the Shihuiyao granites share extremely similar features with tin granites (Lehmann, 1990, 2021).

Several specific geological processes are required for tin granites evolve further into economically mineralized ore bodies, such as magmatic-hydrothermal alteration related to tin-bearing fluid systems and precipitation mechanism caused by changes in physicochemical conditions (Lehmann, 1990; Černý et al., 2005; Sillitoe and Lehmann, 2022). Relatively high TE₁₋₃ values (greater than 1.1) of Shihuiyao granites suggest a probably intense water-rock interaction process (Duan et al., 2021; Zhou et al., 2022). Cassiterites from the pegmatite and leucogranite analyzed by Zhou et al. (2022) demonstrated different element-coupled substitution mechanisms, indicating the differentiation of ore-forming fluids in different lithologies, corresponding to the conclusions concluded from CGMs analysis by Duan et al. (2022). Additionally, during melt-fluid phase separation, tin tends to preferentially enter the fluid phase (Duc-Tin et al., 2007; Zhao et al., 2022a), individual fluid inclusion data indicate that the tin contents in the metallogenic fluids have been reached about 233 ppm during magmatic stages (Table 2), significantly higher than the average contents of 90–120 ppm in melt inclusions of tin-mineralized granites (Zhao et al., 2022b; Zhao et al., 2022c and references therein). Experimental geochemistry results suggest that most of the tin is extracted from the magma by the fluid during the late magmatic crystallization stages, fluids that released from high-ASI magmas have a greater capacity to extract Sn, leading to the generation of Sn-enriched fluids that are more effectively supplied to hydrothermal systems (Zajacz et al., 2008; Zhao et al., 2022a), and this may be the reason for cassiterites generated in the Shihuiyao strong peraluminous granites during magmatic stage.

The composition of FIs, including the magmatic stage and the high-temperature hydrothermal stage (stage 1–3), provides crucial insights into the tin mineralization (e.g., Audébat, 2019; Shu et al., 2021). Specifically, we find that Cs and Rb contents exhibit significant increases, by several orders of magnitude (Fig. 12c), during the evolution of the fluids, indicating an exceptional enrichment process during the magmatic-hydrothermal transition stage. This enrichment process may be attributed to the early phase separation mechanism (like fluid immiscibility or boiling), that occurs during the transformation stage of the preliminary porphyritic granite fluid systems into the leucogranite and greisen fluid systems. Interestingly, the Na + K normalized Sn abundances in the fluid did not change substantially during this phase separation process (Fig. 12c), suggesting that its variation may be constrained by the chlorine in the system. It is widely recognized that Cl is the most crucial complexing anion for Sn in the molten fluid (Sherman et al., 2000; Migdisov and Williams-Jones, 2005; Wang et al., 2019). Thus, our results indicate that the relatively low Cl contents in the fluids, which exhibit a similar variation to that of Sn (Table 2), may restrict the accumulation of tin in the fluids, and this may also explain why Sn/NK did not undergo significant changes. Furthermore, mineralized fluids

obtained from stage 2–3 show similar contents to those in tin mineralized systems (relative to Na, Fig. 12d), which agree with the previous prediction that tin mineralization potential can be estimated by evaluating its concentration in the magma-hydrothermal system (Audébat, 2019; Han et al., 2023). As we observed a gradual increase in Sn/Na with the evolution of the system (an increase in Cs/Na), we thus conclude that the Shihuiyao mining area exhibits a promising prospect for tin mineralization during stage 2–3. And based on the high Sn content in the ore-forming rocks, we postulate that some Sn that has not entered the ore-forming fluids and may be released in subsequent processes.

Furthermore, it is noteworthy that the Shihuiyao ore district is located in the well-known SGXR tin metallogenic belt. The regional tin deposits are mainly hosted in the Permian strata, such as Linxi Formation, the Dashizhai Formation, and Huanggangliang Formation (Zhou and Mao, 2022). The surrounding rocks of the Shihuiyao area belong to the Linxi Formation, with a relatively high background value of tin (~19 ppm, Yang, 1996). Intense water-rock interactions that occur during the late stage of mineralization are highly conducive to the formation of tin-enriched minerals across the contact zone between the mineralized body and the surrounding rocks, as evidenced by the cassiterites with characteristics of hydrothermal alteration that we discovered (Fig. 10c). Moreover, the development of dense faults in the mining area is also conducive to the migration of tin-enriched fluids and the precipitation of Sn-hosted minerals. Considering the similar petrogenetic and metallogenic ages (150–130 Ma) and tectonic background between Shihuiyao and tin deposits in the SGXR, we synthetically believe that the tin mineralization potential of the Shihuiyao area is quite promising, and look forward to further exploration work.

7. Conclusions

Based on fluid inclusion data and new metallogenic ages, we concluded that:

- (1) LA-ICP-MS U-Pb ages of cassiterites suggest the latest Jurassic ore mineralization in Shihuiyao under the extended setting dominated by Paleo-Pacific subduction.
- (2) The primary precipitation mechanism of ore minerals involves the high-temperature and moderately salinity fluid boiling and magma quenching during the magmatic stages, as well as low-temperature, high-salinity fluid mixing and water-rock reactions with the surrounding rocks during the hydrothermal stages.
- (3) The condition of low pressure and shallow intrusion in the early stage is conducive to the quenching of magmas. During the particularly chemical quenching, volatiles disappear or with mineral crystallization, as well as vapor phase migration, promoting the crystallization of columbite-group minerals.
- (4) Shihuiyao granites share remarkable similarities with tin granites, and the mineralized fluid characteristics indicate a promising tin mineralization prospect in this mining area.

Declaration of Competing Interest

The authors declare that they have no known competing financial interests or personal relationships that could have appeared to influence the work reported in this paper.

Data availability

Data will be made available on request.

Acknowledgments

This research was financially supported by the CAGS Research Fund

(Grant No. KK2208), the Science & Technology Fundamental Resources Investigation Program of China (Grant Nos. 2022FY101900 and 2022FY101901) and the National Natural Science Foundation of China (Grant Nos. 41772084, 41302061 and 41820104010). We are grateful to Dr. Zhibin Xiao for assistance during the cassiterite U-Pb dating. Senior geologists Jidong Shao, Wentao Zhao, Zhizhen Gong and Dr. Qiaoping Hu are thanked for their assistance in the field. The authors would like to express their sincere gratitude to Huayong Chen (editor in chief) and two anonymous reviewers for helpful remarks and constructive comments, which have improved the quality of this paper.

Appendix A. Supplementary data

Supplementary data to this article can be found online at <https://doi.org/10.1016/j.oregeorev.2023.105522>.

References

- Akinfiev, N.N., Korzhinskaya, V.S., Kotova, N.P., Redkin, A.F., Zotov, A.V., 2020. Niobium and tantalum in hydrothermal fluids: Thermodynamic description of hydroxide and hydroxofluoride complexes. *Geochim. Cosmochim. Acta* 280, 102–115.
- Allan, M.M., Yardley, B.W.D., Forbes, L.J., Shmulovich, K.I., Banks, D.A., Shepherd, T.J., 2005. Validation of LA-ICP-MS fluid inclusion analysis with synthetic fluid inclusions. *Am. Mineral.* 90, 1767–1775.
- Audéat, A., 2019. The metal content of magmatic-hydrothermal fluids and its relationship to mineralization potential. *Econ. Geol.* 114, 1033–1056.
- Audéat, A., Simon, A.C., 2012. Magmatic Controls on Porphyry Copper Genesis. In: *Geology and Genesis of Major Copper Deposits and Districts of the World: A Tribute to Richard H. Sillitoe*, eds. Jeffrey W. Hedenquist, Michael Harris, Francisco Camus. Society of Economic Geologists, Special Publication 16, pp. 553–572.
- Audéat, A., Günther, D., Heinrich, C.A., 1998. Formation of a magmatic-hydrothermal ore deposit: Insights with LA-ICP-MS analysis of fluid inclusions. *Science* 279 (5359), 2091–2094.
- Audéat, A., Günther, D., Heinrich, C.A., 2000. Magmatic-hydrothermal evolution in a fractionating granite: A microchemical study of the Sn-WF-mineralized Mole Granite (Australia). *Geochim. Cosmochim. Acta* 64 (19), 3373–3393.
- Bodnar, R.J., 1993. Revised equation and table for determining the freezing point depression of H_2O -NaCl solutions. *Geochim. Cosmochim. Acta* 57 (3), 683–684.
- Bowers, T.S., Helgeson, H.C., 1983. Calculation of the thermodynamic and geochemical consequences of nonideal mixing in the system H_2O -CO₂-NaCl on phase relations in geological systems: equation of state for H_2O -CO₂-NaCl fluids at high pressures and temperatures. *Geochim. Cosmochim. Acta* 47, 1247–1275.
- Bozzo, A.T., Chen, J.R., Barduhn, A.J., 1973. The properties of hydrates of chlorine and carbon dioxide. In: Delyannis, A., Delyannis, E. (Eds.), *International Symposium on Fresh Water from the Sea 4th*. Amarolission, Greece, pp. 437–451.
- Brown, P.E., Hagemann, S.G., 1995. Macflincor and its application to fluids in Archean lode-gold deposits. *Geochim. Cosmochim. Acta* 59 (19), 3943–3952.
- Brown, P.E., Lamb, W.M., 1989. P-V-T properties of fluids in the system H_2O -CO₂-NaCl: New graphical presentations and implications for fluid inclusion studies. *Geochim. Cosmochim. Acta* 53 (6), 1209–1221.
- Cerný, P., Blevin, P.L., Cuney, M., London, D., 2005. Granite-related ore deposits. *Soc. Econom. Geol.* 100, 337–370.
- Cerný, P., Novak, M., Chapman, R., 1992. Effects of sillimanite-grade metamorphism and shearing on Nb-Ta oxide minerals in granitic pegmatites: Marsikov, northern Moravia Czechoslovakia. *Can. Mineral.* 30, 699–718.
- Che, X.D., Wu, F.Y., Wang, R.C., Gerdes, A., Ji, W.Q., Zhao, Z.H., Yang, J.H., Zhu, Z.Y., 2015. In situ U-Pb isotopic dating of columbite-tantalite by LA-ICP-MS. *Ore Geol. Rev.* 65, 979–989.
- Chen, X., Zhou, Z., Zhao, J., Gao, X., 2022. Chronology and geochemical composition of cassiterite and zircon from the Maodeng Sn-Cu deposit, Northeastern China: Implications for magmatic-hydrothermal evolution and ore-forming process. *Ore Geol. Rev.* 150, 105159.
- Chevchelov, V.Y., Zaraisky, G.P., Borisovskii, S.E., Borkov, D.A., 2005. Effect of melt composition and temperature on the partitioning of Ta, Nb, Mn, and F between granitic (alkaline) melt and fluorine-bearing aqueous fluid: fractionation of Ta and Nb and conditions of ore formation in rare metal granites. *Petrol.* 13, 305–321.
- Chew, D.M., Sylvester, P.J., Tubrett, M.N., 2011. U-Pb and Th-Pb dating of apatite by LA-ICPMS. *Chem. Geol.* 280 (1-2), 200–216.
- Driesner, T., Heinrich, C.A., 2007. The system H_2O -NaCl. Part I: Correlation formulae for phase relations in temperature-pressure-composition space from 0 to 1000 °C, 0 to 5000 bar, and 0 to 1 XNaCl. *Geochim. Cosmochim. Acta* 71 (20), 4880–4901.
- Duan, Z.P., Jiang, S.Y., Su, H.M., Zhu, X.Y., Zou, T., Cheng, X.Y., 2020. Trace and rare earth elements, and Sr isotopic compositions of fluorite from the Shihuiyao rare metal deposit, Inner Mongolia: Implication for its origin. *Minerals*, 882.
- Duan, Z.P., Jiang, S.Y., Su, H.M., Zhu, X.Y., Zou, T., Cheng, X.Y., 2021. Geochronological and geochemical investigations of the granites from the giant Shihuiyao Nb-Ta-Bi deposit, Inner Mongolia: Implications for magma source, magmatic evolution, and rare metal mineralization. *Lithos* 400–401, 1–15.
- Duan, Z.-P., Jiang, S.-Y., Su, H.-M., Zhu, X.-Y., Zou, T., 2022. Nb-Ta oxides as recorders of hydrothermal activity in the Shihuiyao Rb-Nb-Ta-(Be-Li) deposit, Inner Mongolia. *NE China. Ore Geol. Rev.* 150, 105149.
- Duan, X.Z., Shi, H., Tan, K.X., Xie, Y.S., Chen, L., Han, S.L., Hu, Y., Feng, Z.G., Zhang, Y.Q., Guo, H.F., Jiang, L., 2016. Geology and genesis of the granitic niobium-tantalum-rubidium deposit in Shihuiyao area, Inner Mongolia. *Geol. Resour.* 25, 32–40 in Chinese with English abstracts.
- Duc-Tin, Q., Audéat, A., Keppler, H., 2007. Solubility of tin in (Cl, F)-bearing aqueous fluids at 700°C, 140 MPa: A LA-ICP-MS study on synthetic fluid inclusions. *Geochim. Cosmochim. Acta* 71, 3323–3335.
- Fan, H.R., Zhai, M.G., Xie, Y.H., Yang, J.H., 2003. Ore-forming fluids associated with granite-hosted gold mineralization at the Sanshandao deposit, Jiaodong gold province. *China. Miner. Deposita* 38 (6), 739–750.
- Ge, W.C., Wu, F.Y., Zhou, C.Y., Zhang, J.H., 2005. Zircon U-Pb ages and its significance of the Mesozoic granites in the Wulanhaote Region, central Great Xing'an Range. *Acta Petrol. Sin.* 15, 396–407 in Chinese with English abstract.
- Guillong, M., Latkoczy, C., Seo, J.H., Gunther, D., Heinrich, C.A., 2008. Determination of sulfur in fluid inclusions by laser ablation ICP-MS. *J. Anal. At. Spectrom.* 23, 1581–1589.
- Hall, D.L., Sternier, S.M., Bodnar, R.J., 1988. Freezing point depression of NaCl-KCl-H₂O solutions. *Econ. Geol.* 83, 197–202.
- Han, L., Pan, J.Y., Ni, P., Chen, H., 2023. Cassiterite deposition induced by cooling of a single-phase magmatic fluid: Evidence from SEM-CL and fluid inclusion LA-ICP-MS analysis. *Geochim. Cosmochim. Acta* 342, 108–127.
- Heinrich, C.A., Pettke, T., Halter, W.E., Aigner-Torres, M., Audéat, A., Günther, D., Hattendorf, B., Bleiner, D., Guillong, M., Horn, I., 2003. Quantitative multi-element analysis of minerals, fluid and melt inclusions by laser-ablation inductively-coupled plasma mass-spectrometry. *Geochim. Cosmochim. Acta* 67 (18), 3473–3497.
- Hu, T., Sun, Z., Liu, G., Yu, H., Wang, C., Zhao, Z., Sun, J., 2020. Zircon U-Pb dating, Lu-Hf isotopic composition and geological significance of granites in the Haobugao Pb-Zn deposit, southern Great Xing'an Range. *China. Arabian J. Geosci.* 13, 1–22.
- Ishihara, S., 1981. The granitoid series and mineralization. *Econ. Geol.* 75th Anniv. Vol. 458–484.
- Jahn, B.M., Wu, F.Y., Chen, B., 2000. Massive granitoid generation in central Asia: Nd isotopic evidence and implication for continental growth in the Phanerozoic. *Episodes* 23, 82–92.
- Jiang, S.Y., Wen, H.J., Xu, C., Wang, Y., Su, H.M., Sun, W.D., 2019. Earth sphere cycling and enrichment mechanism of critical metals: major scientific issues for future research. *Bull. Natl. Nat. Sci. Found. China* 33, 112–118 in Chinese with English abstract.
- Lan, T.G., Hu, R.Z., Bi, X.W., Mao, G.J., Wen, B.J., Liu, L., Chen, Y.H., 2018. Metasomatized asthenospheric mantle contributing to the generation of Cu-Mo deposits within an intracontinental setting: a case study of the ~128 Ma Wangjiazhuang Cu-Mo deposit, eastern North China Craton. *J. Asian Earth Sci.* 160, 460–489.
- Lehmann, B., 1990. Metallogeny of Tin. Springer, Berlin, p. 211.
- Lehmann, B., 2021. Formation of tin ore deposits: A reassessment. *Lithos* 402–403, 105756.
- Lehmann, B., Zoheir, B.A., Neymark, L.A., Zeh, A., Emam, A., Radwan, A.M., Zhang, R.Q., Moscati, R.J., 2020. Monazite and cassiterite U-Pb dating of the Abu Dabbab rare-metal granite, Egypt: Late Cryogenian metalliferous granite magmatism in the Arabian-Nubian Shield. *Gondwana Res.* 84, 71–80.
- Li, Y., Brouwer, F.M., Xiao, W., Zheng, J., 2017c. A Paleozoic fore-arc complex in the eastern Central Asian Orogenic Belt: Petrology, geochemistry and zircon U-Pb-Hf isotopic composition of paragneisses from the Xilingol Complex in Inner Mongolia, China. *Gondwana Res.* 47, 323–341.
- Li, S., Chung, S.-L., Wang, T., Wilde, S.A., Chu, M.-F., Guo, Q.-Q., 2017a. Tectonic significance and geodynamic processes of large-scale Early Cretaceous granitoid magmatic events in the southern Great Xing'an Range, North China. *Tectonics* 36 (4), 615–633.
- Li, S., Chung, S.L., Wang, T., Wilde, S.A., Chu, M.F., Pang, C.J., Guo, Q.Q., 2018. Water-fluxed crustal melting and petrogenesis of large-scale Early Cretaceous intracontinental granitoids in the southern Great Xing'an Range, North China. *Geol. Soc. Am. Bull.* 130, 580–597.
- Li, S.H., Li, J.K., Chou, I.M., Jiang, L., Ding, X., 2017b. The formation of the Yichun Ta-Nb deposit, South China, through fractional crystallization of magma indicated by fluid and silicate melt inclusions. *J. Asian Earth Sci.* 137, 180–193.
- Li, J., Liu, C., Liu, X., Li, P., Huang, Z., Zhou, F., 2019. Tantalum and niobium mineralization from F- and Cl-rich fluid in the lepidolite-rich pegmatite from the Renli deposit in northern Hunan, China: Constraints of fluid inclusions and lepidolite crystallization experiments. *Ore Geol. Rev.* 115, 103187.
- Liang, L.H., Peng, Z.A., Wang, M., Zhang, F., Liu, H., Guo, T.F., Huang, D.J., 2012. Characteristics of mineralizing fluid inclusion in Sn-Nb-Ta polymetallic deposit in Limu of Guangxi. *Miner. Resour. Geol.* 26, 502–510 in Chinese with English abstract.
- Linnen, R.L., Cuney, M., 2005. Granite-related rare-element deposits and experimental constraints on Ta-Nb-W-Sn-Zr-Hf mineralization. In: Linnen RL, Samson IM (eds) Rare-element geochemistry and mineral deposits. GAC Short Course Notes 17, 4568.
- Linnen, R.L., Samson, I.M., Williams-Jones, A.E., Chakhmouradian, A.R., 2014. In: *Treatise on Geochemistry*. Elsevier, pp. 543–568.
- Liu, W., Pan, X.F., Xie, L.W., Li, H., 2007. Sources of material for the Linxi granitoids, the southern segment of the Da Hinggan Mts.: when and how continental crust grew? *Acta Petrol. Sin.* 23, 441–460 in Chinese with English abstract.
- London, D., 2008. Pegmatites. *Can. Mineral. Spec. Publ.* 10, 347.
- Mangas, J., Arribas, A., 1987. Fluid inclusion study in different types of tin deposits associated with the Hercynian granites of western Spain. *Chem. Geol.* 61 (1-4), 193–208.

- Mao, J.W., Ouyang, H.G., Song, S.W., Santosh, M., Yuan, S.D., Zhou, Z.H., Zheng, W., Liu, H., Liu, P., Cheng, Y.B., Chen, M.H., 2019. Geology and metallogeny of tungsten and tin deposits in China. *Econ. Geol. (Spec. Publ.)* 22, 411–482.
- Meffre, S., Large, R.R., Scott, R., Woodhead, J., Chang, Z., Gilbert, S.E., Danyushevsky, L.V., Maslenikov, V., Hergt, J.M., 2008. Age and pyrite Pb-isotopic composition of the giant Sukhoi Log sediment-hosted gold deposit. *Russia. Geochim. Cosmochim. Acta* 72 (9), 2377–2391.
- Mernagh, T.P., Mavrogenes, J., 2019. Significance of high temperature fluids and melts in the Grasberg porphyry copper-gold deposit. *Chem. Geol.* 508, 210–224.
- Migdisov, A.A., Williams-Jones, A.E., 2005. An experimental study of cassiterite solubility in HCl-bearing water vapour at temperatures up to 350°C: Implications for tin ore formation. *Chem. Geol.* 217, 29–40.
- Mulja, T., Williams-Jones, A.E., 2018. The physical and chemical evolution of fluids in rare-element granitic pegmatites associated with the Lacorne pluton, Québec, Canada. *Chem. Geol.* 493, 281–297.
- Muntean, J.L., Einaudi, M.T., 2001. Porphyry-epithermal transition: Maricunga belt, northern Chile. *Econ. Geol.* 96, 743–772.
- Nakano, T., Urabe, T., 1989. Calculated compositions of fluids released from a crystallizing granitic melt: Importance of pressure on the genesis of ore forming fluid. *Geochem. J.* 23 (6), 307–319.
- Neymark, L.A., Holm-Denoma, C.S., Moscati, R.J., 2018. In situ LA-ICPMS U-Pb dating of cassiterite without a known-age matrix-matched reference material: Examples from worldwide tin deposits spanning the Proterozoic to the Tertiary. *Chem. Geol.* 483, 410–425.
- Ouyang, H., Mao, J., Santosh, M., Wu, Y., Hou, L., Wang, X., 2014. The Early Cretaceous Weilasituo Zn–Cu–Ag vein deposit in the southern Great Xing'an Range, northeast China: Fluid inclusions, H, O, S, Pb isotope geochemistry and genetic implications. *Ore Geol. Rev.* 56, 503–515.
- Ouyang, H., Mao, J., Zhou, Z., Su, H., 2015. Late Mesozoic metallogeny and intracontinental magmatism, southern Great Xing'an Range, northeastern China. *Gondwana Res.* 27 (3), 1153–1172.
- Pan, J.Y., Ni, P., Wang, R.C., 2019. Comparison of fluid processes in coexisting wolframite and quartz from a giant vein-type tungsten deposit, South China: Insights from detailed petrography and LA-ICP-MS analysis of fluid inclusions. *Am. Mineral.* 104, 1092–1116.
- Pekov, I.V., Kononkova, N.N., 2010. Rubidium mineralization in Rare Element granitic pegmatites of the voron'i tundras, Kola Peninsula, Russia. *Geochem. Int.* 48 (7), 695–713.
- Phillips, G.N., Evans, K.A., 2004. Role of CO₂ in the formation of gold deposits. *Nature* 429 (6994), 860–863.
- Pichavant, M., Kontak, D.J., Herrera, J.V., Clark, A.H., 1988. The Miocene-Pliocene Macusani volcanics, SE Peru. *Contrib. Mineral. Petrol.* 100 (3), 300–324.
- Pollard, P.J., 2021. The Yichun Ta-Sn-Li deposit, South China: evidence for extreme chemical fractionation in F-Li-P-rich magma. *Econ. Geol.* 116, 453–469.
- Potter, R.W., Babcock, R.S., Brown, D.L., 1977. A new method for determining the solubility of salts in aqueous solutions at elevated temperatures. *J. Res. U.S. Geol. Surv.* 5, 389–395.
- Prichard, J., 2013. The Geochemistry and Geochronology of Cassiterite from the New England Fold Belt, NSW. BSC honours thesis. Australian National University.
- Qin, K.Z., Zhao, J.X., Fan, H.R., Tang, D.M., Li, G.M., Yu, K.L., Cao, M.J., Su, B.X., 2021. On the ore-forming depth and possible maximum vertical extension of the major type ore deposits. *Earth Sci. Front.* 28, 271–294 in Chinese with English abstract.
- Rajabpour, S., Jiang, S.Y., Lehmann, B., Abedini, A., Gregory, D.D., 2018. Fluid inclusion and O-H-C isotopic constraints on the origin and evolution of ore-forming fluids of the Cenozoic volcanic-hosted Kuh-Pang copper deposit. *Central Iran. Ore Geol. Rev.* 94, 277–289.
- Roedder, E., 1984. Fluid inclusions. *Rev. Mineral.* 12, 644.
- Roedder, E., Bodnar, R.J., 1980. Geologic pressure determinations from fluid inclusion studies. *Annu. Rev. Earth Planet. Sci.* 8 (1), 263–301.
- Rottier, B., Kouzmanov, K., Bouvier, A., Baumgartner, L., Walle, M., Rezeau, H., Bendezu, R., Fontbote, L., 2016. Heterogeneous melt and hyper saline liquid inclusions in shallow porphyry type mineralization as markers of the magmatic-hydrothermal transition (Cerro de Pasco district, Peru). *Chem. Geol.* 447, 93–116.
- Runyon, S.E., Steele-MacInnis, M., Seedorff, E., Lecumberri-Sanchez, P., Mazdab, F.K., 2017. Coarse muscovite veins and alteration deep in the Yerington batholith, Nevada: insights into fluid exsolution in the roots of porphyry copper systems. *Miner. Deposita* 52 (4), 463–470.
- Samson, I.M., Williams-Jones, A.E., Ault, K.M., Gagnon, J.E., Fryer, B.J., 2008. Source of fluids forming distal Zn-Pb-Ag skarns: Evidence from laser ablation-inductively coupled plasma–mass spectrometry analysis of fluid inclusions from El Mochito, Honduras. *Geology* 36 (12), 947.
- Sengör, A.M.C., Natal'in, B.A., Burtman, V.S., 1993. Evolution of the Altai tectonic collage and Palaeozoic crustal growth in Eurasia. *Nature* 364, 299–307.
- Shao, J.A., Mu, B.L., Zhu, H.Z., Zhang, L.Q., 2010. Material source and tectonic settings of the Mesozoic mineralization or the Da Hinggan Mts. *Acta Petrol. Sin.* 26, 649–656 in Chinese with English abstract.
- Shepherd, T.J., Rankin, A.H., Alderton, D.H.M., 1985. A Practical Guide to Fluid Inclusion Studies. Blackie and Sons Ltd., Glasgow, p. 239.
- Sherman, D.M., Ragnarsdóttir, K.V., Oelkers, E.H., Collins, C.R., 2000. Speciation of tin (Sn²⁺ and Sn⁴⁺) in aqueous Cl solutions from 25°C to 350°C: an in situ EXAFS study. *Chem. Geol.* 167, 169–176.
- Shi, G.H., Liu, D.Y., Zhang, F.Q., Jian, P., Miao, L.C., Shi, Y.R., Tao, H., 2003. SHRIMP U-Pb zircon geochronology and its implications on the Xilin Gol Complex, Inner Mongolia. *China. Chinese Sci. Bull.* 48, 2742–2748.
- Shu, Q., Chang, Z., Hammerli, J., Lai, Y., Huizenga, J.M., 2017. Composition and evolution of fluids forming the Baiyinno' er Zn-Pb skarn deposit, northeastern China: Insights from laser ablation ICP-MS study of fluid inclusions. *Econ. Geol.* 112, 1441–1460.
- Shu, Q., Chang, Z., Mavrogenes, J., 2021. Fluid compositions reveal fluid nature, metal deposition mechanisms, and mineralization potential: An example at the Haobugao Zn-Pb skarn, China. *Geology* 49, 473–477.
- Sillitoe, R.H., Lehmann, B., 2022. Copper-rich tin deposits. *Min. Depos.* 57, 1–11.
- Steele-MacInnis, M., Lecumberri-Sanchez, P., Bodnar, R.J., 2012. HOKIEFLINCS_H2O-NACL: A Microsoft Excel spreadsheet for interpreting microthermometric data from fluid inclusions based on the PVTX properties of H₂O–NaCl. *Comput. Geosci.* 49, 334–337.
- Su, H.M., Jiang, S.Y., Zhu, X.Y., Duan, Z.P., Huang, X.K., Zou, T., 2021. Magmatic-hydrothermal processes and controls on rare-metal enrichment of the Baerzhe peralkaline granitic pluton, inner Mongolia, northeastern China. *Ore Geol. Rev.* 131, 103984.
- Sun, Y., Wang, R.J., Li, J.K., Zhao, Z., 2015. ⁴⁰Ar–³⁹Ar dating of the muscovite and regional exploration prospect of Shihuiyao rubidium-multi-metal deposit, Selenhot, Inner Mongolia. *Geol. Rev.* 61, 463–468 in Chinese with English abstract.
- Sun, Y., 2013. Study on magmatic fluid evolution and mineralization of rare metal granites in the middle-southern Great Xing'an Range. Master thesis. Beijing: Peking University in Chinese with English abstract.
- Tapster, S., Bright, J.W.G., 2020. High-precision ID-TIMS cassiterite U-Pb systematics using a low-contamination hydrothermal decomposition: implications for LA-ICP-MS and ore deposit geochronology. *Geochronology* 2, 425–441.
- Timofeev, A., Migdisov, A.A., Williams-Jones, A.E., 2015. An experimental study of the solubility and speciation of niobium in fluoride-bearing aqueous solutions at elevated temperature. *Geochim. Cosmochim. Acta* 158, 103–111.
- Vasyukova, O., Williams-Jones, A.E., 2014. Fluoride–silicate melt immiscibility and its role in REE ore formation: Evidence from the Strange Lake rare metal deposit, Quebec–Labrador, Canada. *Geochim. Cosmochim. Acta* 139, 110–130.
- Wang, T., Guo, L., Zhang, L., Yang, Q., Zhang, J., Tong, Y., Ye, K., 2015. Timing and evolution of Jurassic-Cretaceous granitoid magmatism in the Mongol-Okhotsk belt and adjacent areas, NE Asia: Implications for transition from contractional crustal thickening to extensional thinning and geodynamic settings. *J. Asian Earth Sci.* 97, 365–392.
- Wang, D., Mathur, R., Powell, W., Godfrey, L., Zheng, Y., 2019. Experimental evidence for fractionation of tin chlorides by redox and vapor mechanisms. *Geochim. Cosmochim. Acta* 250, 209–218.
- Wang, T., Tong, Y., Xiao, W., Guo, L., Windley, B.F., Donskaya, T., Li, S., Tserendash, N., Zhang, J., 2022. Rollback, scissor-like closure of the Mongol-Okhotsk Ocean and formation of an orocline: magmatic migration based on a large archive of age data. *Natl. Sci. Rev.* 9, nwab210.
- Wilde, S.A., 2015. Final amalgamation of the Central Asian Orogenic Belt in NE China: Paleo-Asian Ocean closure versus Paleo-Pacific plate subduction–A review of the evidence. *Tectonophysics* 662, 345–362.
- Wilde, S.A., Zhou, J.B., 2015. The late Paleozoic to Mesozoic evolution of the eastern margin of the Central Asian Orogenic Belt in China. *J. Asian Earth Sci.* 113, 909–921.
- Wilkinson, J.J., 2001. Fluid inclusions in hydrothermal ore deposits. *Lithos* 55, 229–272.
- Wolf, M., Romer, R.L., Franz, L., López-Moro, F.J., 2018. Tin in granitic melts: The role of melting temperature and protolith composition. *Lithos* 310, 20–30.
- Wu, G., Liu, R.L., Chen, G.Z., Li, T.G., Li, R.H., Li, Y.L., Yang, F., Zhang, T., 2021. Mineralization of the Weilasituo rare metal-tin-polymerite ore deposit in Inner Mongolia: Insights from fractional crystallization of granitic magmas. *Acta Petrol. Sin.* 37, 637–664 in Chinese with English abstract.
- Wu, M.Q., Samson, I.M., Zhang, D.H., 2018. Textural features and chemical evolution in Ta-Nb oxides: Implications for deuterium rare-metal mineralization in the Yichun granite-marginal pegmatite, southeastern China. *Econ. Geol.* 11, 937–960.
- Wu, F.Y., Sun, D.Y., Ge, W.C., Zhang, Y.B., Grant, M.L., Wilde, S.A., Jahn, B.M., 2011. Geochronology of the Phanerozoic granitoids in northeastern China. *J. Asian Earth Sci.* 41, 1–30.
- Xi, B.B., Zhang, D.H., Zhou, L.M., Zhang, W.H., Wang, C., 2008. Characteristics of Ore-forming Fluid Evolution in Dajishan Tungsten Deposit, Quannan County, Jiangxi. *Acta Geol. Sin.* 7, 956–966 in Chinese with English abstract.
- Xiao, W.J., Windley, B., Huang, B.C., Han, C.M., Yuan, C., Chen, H.L., Sun, M., Sun, S., Li, J.L., 2009. End-Permian to mid-Triassic termination of the accretionary processes of the southern Altai: implications for the geodynamic evolution, Phanerozoic continental growth and metallogeny of Central Asia. *Int. J. Earth Sci.* 98, 1189–1217.
- Xie, L., Wang, R.C., Hu, H., Che, X.D., Xiang, L., 2019. Li-Nb-Ta mineralization in the Jurassic Yifeng granite-aplite intrusion within the Neoproterozoic Jiuling batholith, south China: A fluid-rich and quenching ore-forming process. *J. Asian Earth Sci.* 185, 104047.
- Xu, W.L., Pei, F.P., Wang, F., Meng, E., Ji, W.Q., Yang, D.B., Wang, W., 2013. Spatial-temporal relationships of Mesozoic volcanic rocks in NE China: Constraints on tectonic overprinting and transformations between multiple tectonic regimes. *J. Asian Earth Sci.* 74, 167–193.
- Xu, W.L., Sun, C.Y., Tang, J., Nuan, J.F., Wang, F., 2019. Basement Nature and Tectonic Evolution of the Xing'an-Mongolian Orogenic Belt. *Earth Sci.* 44, 1620–1646 in Chinese with English abstract.
- Yang, G.F., 1996. Geological formation and ore-controlling process of Permian system in the southern part of Dahingganling, Inner Mongolia. *Miner. Resour. Geol.* 2, 49–54 in Chinese with English abstract.
- Yin, L., Pollard, P.J., Shouxi, H., Taylor, R.G., 1995. Geologic and geochemical characteristics of the Yichun Ta-Nb-Li deposit, Jiangxi Province, South China. *Econ. Geol.* 90, 577–585.
- Yuan, S.D., Peng, J.T., Hao, S., Li, H.M., Geng, J.Z., Zhang, D.L., 2011. In situ LA-MC-ICP-MS and ID-TIMS U-Pb geochronology of cassiterite in the giant Furong tin deposit,

- Hunan Province, South China: new constraints on the timing of tin-polymetallic mineralization. *Ore Geol. Rev.* 43, 235–242.
- Zajacz, Z., Halter, W.E., Pettke, T., Guillong, M., 2008. Determination of fluid/melt partition coefficients by LA-ICPMS analysis of co-existing fluid and silicate melt inclusions: controls on element partitioning. *Geochim. Cosmochim. Acta* 72, 2169–2197.
- Zhai, D., Liu, J., Cook, N.J., Wang, X., Yang, Y., Zhang, A., Jiao, Y., 2019b. Mineralogical, textural, sulfur and lead isotope constraints on the origin of Ag-Pb-Zn mineralization at Bianjiadayuan, Inner Mongolia, NE China. *Miner. Deposita* 54, 47–66.
- Zhai, M.G., Wu, F.Y., Hu, R.Z., Jiang, S.Y., Li, W.C., Wang, R.C., Wang, D.H., Qi, T., Qin, K.Z., Wen, H.J., 2019a. Critical metal mineral resources: current research status and scientific issues. *Bull. Natl. Nat. Sci. Found. China* 33, 106–111 in Chinese with English abstract.
- Zhang, J.H., Gao, S., Ge, W.C., Wu, F.Y., Yang, J.H., Wilde, S.A., Li, M., 2010. Geochronology of the Mesozoic volcanic rocks in the Great Xing'an Range, Northeast China: implications for subduction-induced delamination. *Chem. Geol.* 276, 144–165.
- Zhang, D.L., Peng, J.T., Hu, R.Z., Yuan, S.D., Zheng, D.S., 2011. The closure of U-Pb isotope system in cassiterite and its reliability for dating. *Geol. Rev.* 57, 549–554 in Chinese with English abstract.
- Zhao, P.L., Chu, X., Williams-Jones, A.E., Mao, J.W., Yuan, S.D., 2022c. The role of phyllosilicate partial melting in segregating tungsten and tin deposits in W-Sn metallogenic provinces. *Geology* 50, 121–125.
- Zhao, P., Zajacz, Z., Tsay, A., Yuan, S., 2022b. Magmatic-hydrothermal tin deposits form in response to efficient tin extraction upon magma degassing. *Geochim. Cosmochim. Acta* 316, 331–346.
- Zhao, J.Q., Zhou, Z.H., Ouyang, H.G., Chen, B.Q., Liu, W.J., Yang, F., 2022a. Zircon U-Pb age and geochemistry of quartz syenite porphyry in Shuangjianzishan Ag-Pb-Zn (Sn) deposit, Inner Mongolia, and their geological implications. *Miner. Deposits* 41, 324–344 in Chinese with English abstract.
- Zhou, Z.H., Mao, J.W., Lyckberg, P., 2012. Geochronology and isotopic geochemistry of the A-type granites from the Huanggang Sn-Fe deposit, southern Great Hinggan Range, NE China: implication for their origin and tectonic setting. *J. Asian Earth Sci.* 49, 272–286.
- Zhou, Z.H., Mao, J.W., 2022. Metallogenic patterns and ore deposit model of the tin polymetallic deposits in the southern segment of Great Xing'an Range. *Earth Sci. Front.* 29, 176 in Chinese with English abstract.
- Zhou, Z.H., Breiter, K., Wilde, S.A., Gao, X., Burnham, A.D., Ma, X.H., Zhao, J.Q., 2022. Ta-Nb mineralization in the shallow-level highly-evolved P-poor Shihuiyao granite, Northeast China. *Lithos* 416–417, 1–21.